

EXPERIMENTAL STUDY OF USING A PATTERNED
MICROTEXTURE TO REDUCE FRICTION
IN PROSTHETIC HIP JOINTS

by

Anthony Chyr

A thesis submitted to the faculty of
The University of Utah
in partial fulfillment of the requirements for the degree of

Master of Science

Department of Mechanical Engineering

The University of Utah

August 2014

Copyright © Anthony Chyr 2014

All Rights Reserved

THE UNIVERSITY OF UTAH GRADUATE SCHOOL

STATEMENT OF THESIS APPROVAL

The thesis of _____ **Anthony Chyr** _____

has been approved by the following supervisory committee members:

_____ **Bart Raeymaekers** _____, Chair 03/14/2014
Date Approved

_____ **Rebecca Brannon** _____, Member 03/14/2014
Date Approved

_____ **A. K. Balaji** _____, Member 03/14/2014
Date Approved

And by _____ **Timothy Ameal** _____, Chair of the
Department of _____ **Mechanical Engineering** _____,

and by David B. Kieda, Dean of The Graduate School.

ABSTRACT

More than 285,000 total hip replacement (THR) surgeries are performed in the United States each year. Most prosthetic hip joints consist of a cobalt-chromium (CoCr) femoral head that articulates with a polyethylene acetabular component lubricated with synovial fluid. The statistical survivorship of these metal-on-polyethylene prosthetic hip joints declines significantly after 10 to 15 years of use, primarily as a result of polyethylene wear and wear debris incited disease. The current engineering paradigm to increase the longevity of prosthetic hip joints is to manufacture ultra-smooth articulating surfaces. In contrast, this work shows that adding a patterned microtexture to the ultra-smooth CoCr femoral head reduces friction when articulating with the polyethylene acetabular liner. The microtexture increases the load-carrying capacity and the thickness of the joint lubricant film, which reduces contact between the articulating surfaces. As a result, friction and wear is reduced. A lubrication model is used to design the geometry of the patterned microtexture, and we experimentally demonstrate reduced friction for the microtextured compared to conventional smooth surrogate prosthetic hip joints.

TABLE OF CONTENTS

ABSTRACT	iii
LIST OF TABLES	vi
LIST OF FIGURES	vii
ACKNOWLEDGEMENTS	ix
Chapters	
1. INTRODUCTION	1
1.1 Significance	1
1.2 Terminology.....	3
1.3 History	4
1.4 Current state of research	5
1.5 Approach.....	8
2. PATTERNED MICROTTEXTURE DESIGN	10
2.1 Model	10
2.2 Simulation results	12
3. EXPERIMENTAL APPARATUS	14
3.1 Friction and wear tests	14
3.1.1 Pin-on-disk experiment	14
3.1.2 Prosthetic hip joint simulator	15
3.1.3 Hybrid experimental apparatus	17
3.2 Concept	18
3.3 Mechanical design	19
3.4 Specimen design	22
3.5 Instrumentation	23
3.6 Friction measurements	25
3.7 Limitations	27
4. SPECIMENS	30
4.1 Manufacturing process.....	30

4.2 Characterization	31
5. EXPERIMENTAL METHODOLOGY	35
5.1 Example experiment	35
5.2 Repeatability and reliability of the experiments	36
6. RESULTS AND DISCUSSION	38
7. CONCLUSION	43
Appendices	
A. DATA ACQUISITION.....	45
B. DATA REDUCTION	48
REFERENCES	51

LIST OF TABLES

- 6.1 Average kinematic friction coefficient for different microtexture designs and contact pressures. The color coding (green – red) is used to visualize the magnitude of the relative values of the friction coefficient. 39
- 6.2 Different microtexture designs, showing the percentage of the 1 Hz kinematic cycle during which the microtextured CoCr specimen has a lower coefficient of friction than the smooth CoCr specimen, for different values of constant bearing contact pressure. The color coding (green – red) is used to visualize the magnitude of the relative benefit of each microtexture compared to the smooth CoCr specimen. 40

LIST OF FIGURES

1.1 Age distribution of patients who received a primary hip replacement in 2006 in the United States.....	2
1.2 Most common reasons for prosthetic hip joint failure.....	3
1.3 Metal-on-polyethylene prosthetic hip joint.....	3
1.4 Metal-on-polyethylene prosthetic hip joint with a patterned microtexture on the CoCr femoral head.....	6
1.5 Schematic of natural hip joint with the articular cartilage on the femoral head articulating against the articular cartilage in the acetabulum.	8
1.6 Sliding interface between femoral head and acetabular component.....	9
2.1 Schematic of the lubrication model showing (a) cross-sectional view and (b) top view.....	10
2.2 Non-dimensional load-carrying capacity per unit area as a function of texture density and texture aspect ratio for $\lambda = 5.94 \times 10^{-4}$ and $\delta = 0.01$	13
3.1 Six degrees of freedom of the prosthetic hip joint: AP, ML, and PD translations and FE, IE, and AA rotations.....	16
3.2 Concept of the apparatus, showing two articulating prosthetic hip joint bearing surfaces subject to a torque moment M_t and normal load for N (a) cylindrical on flat, (b) convex cylindrical on concave cylindrical, and (c) fully conformal contact.....	18
3.3 Mechanical design of the experimental apparatus.....	20
3.4 Implementation of the experimental apparatus (a) overview picture, (b) detail of the cylindrical CoCr cylinder mounted on the reciprocating shaft in the reservoir, and (c) detail of the interacting CoCr and UHMWPE articulating surfaces.	20
3.5 Detail of the load mechanism, showing the threaded rod and ACME nut, as well as the precision shafts with compression springs that create the load.	21

3.6 Typical examples of bearing pair specimens, showing (a) CoCr cylindrical surface 1, mounted on reciprocating shaft and (b) UHMWPE surface 2 mounted on the loading mechanism.	23
3.7 Instrumentation of the normal load mechanism, FE rotation drive mechanism, and data input/output.	24
3.8 Typical friction measurement of a convex CoCr cylinder articulating against a conformal concave UHMWPE specimen (contact span is 90°), (a) kinematic input cycle, (b) normal load, (c) normalized torque, and (d) normalized friction coefficient, as a function of time.	26
3.9 Typical friction measurement of a convex CoCr cylinder articulating against a flat UHMWPE specimen, (a) kinematic input cycle, (b) normal load, (c) normalized torque, and (d) normalized friction coefficient, as a function of time.	26
4.1 Laser surface texturing process.	31
4.2 Optical microscope and white light interferometer images of each of the four patterned microtexture designs, manufactured on cylindrical CoCr specimens (ASTM F1537-08), showing the results of the LST process.	33
4.3 Smooth cylindrical CoCr specimen (a) photograph and (b) white light interferometer image of the articulating surface.	34
4.4 UHMWPE specimen (a) photograph and (b) white light interferometer image of the articulating surface.	34
5.1 Typical experiment showing input kinematic cycle and output friction coefficient as a function of time.	36
A.1 Schematic of the data recording procedure where analog voltage signals from normal and torque load cells are quantized by the Sensoray 626 PCI card, associated with the time measured by the CPU clock, and electronically archived by an in-house DAQ application.	46
B.1 Schematic of a typical data reduction procedure where the electronically archived datasets are loaded into a structured array in MATLAB, filtered for electrical noise, posttriggered, compensated for inertial and support bearing effects, and displayed.	49
B.2 Detail of the removal procedure for the inertial and support bearing effects.	49

ACKNOWLEDGEMENTS

This work is partially funded through NSF award #1227869, NIH award #1R41AR064095-01 and a University of Utah Technology Commercialization grant. I also acknowledge partial funding through an Undergraduate Research Opportunity Program (UROP) award from the University of Utah, and through the Society of Tribologists and Lubrication Engineers (STLE) E. Richard Booser Presidential Award.

I thank Dr. Ronald L. Jacobsen and those at Mound Laser and Photonics Center (MLPC) for providing the CoCr specimens, and Dr. Anthony P. Sanders for teaching me how to operate a White Light Interferometer (WLI) and for providing the UltraHigh Molecular Weight Polyethylene (UHMWPE) specimens. I acknowledge the assistance of Mr. Daniel Cowan for designing the experimental apparatus used throughout this work, and Mr. Mingfeng Qiu for providing the simulation results used to optimize the patterned microtexture. For without their contributions this work would not have been possible.

I thank Dr. Rebecca Brannon for her advice and encouragement. For without her help, I would not have been introduced to Dr. Bart Raeymaekers, and would not have found such an interesting topic of research.

Finally, I thank Dr. Bart Raeymaekers for providing funding when funding was needed; advice when advice was needed; and for his patience, critique, and support in taking me under his wing and teaching me to fish.

Chapters 1, 2, 4, 5, 6, and 7 are adapted from the material in “A Patterned

Microtexture to Reduce Friction and Increase Longevity of Prosthetic Hip Joints” by Anthony Chyr, Mingfeng Qiu, Jared Speltz, Ronald L. Jacobsen, Anthony P. Sanders, and Bart Raeymaekers – published in *Wear*, vol. 315, pp. 51-57, 2014.

Chapter 1 is adapted from the material in “Designing Prosthetic Knee Joints with Bio-inspired Bearing Surfaces” by Mingfeng Qiu, Anthony Chyr, Anthony P. Sanders, and Bart Raeymaekers – published in *Tribology International*, vol. 77, pp. 106-110, 2014.

Chapter 3 is adapted from the material in “A Hybrid Apparatus for Friction and Accelerated Wear Testing of Total Hip Replacement Bearing Materials” by Anthony Chyr, Anthony P. Sanders, and Bart Raeymaekers – published in *Wear*, vol. 308, pp. 54-60, 2013.

CHAPTER 1

INTRODUCTION *

1.1 Significance

More than 285,000 total hip replacement (THR) surgeries are performed in the United States each year to treat degenerative joint diseases that cause pain and disability [1]. This number is projected to increase to 572,000 by 2030 [2], which has been cited to have “important implications” to the growing cost of healthcare in the United States [3]. Revision surgeries are performed when the primary THR surgery must be replaced, and are often much more technically demanding than primary surgeries. Up to 17.5% of prosthetic hips are expected to undergo revision surgeries [3], and those who undergo revision surgeries are six times more likely to undergo re-revision surgeries [4]. The statistical survivorship of prosthetic hip joints is 90 – 95% at 10 years, but declines dramatically after 15 years [5, 6]. Figure 1.1 shows the age distribution of THR patients in 2006 in the US with the majority of patients between the ages of 55 and 74 [6]. However, with the increased prevalence of obesity, the majority of THR surgeries today are performed on patients less than 65 years of age [6, 7]. Consequently, these two factors strongly contribute to the cost of healthcare in the United States as THR surgeries are performed on a younger and larger fraction of the population than ever before [3, 6, 7].

* This chapter is adapted from the material in [48, 59].

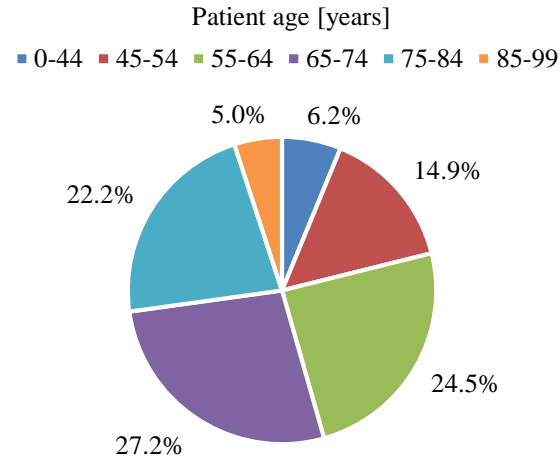


Figure 1.1 Age distribution of patients who received a primary hip replacement in 2006 in the United States. (Data source [6].)

Figure 1.2 shows the most important failure mechanisms of metal-on-polyethylene (MOP) prosthetic hip joints, which are the most common in the United States. Failure due to instability/dislocation and infection typically occur early in the life of the prosthetic joint arising from the quality of the surgery [8]. However, failure due to mechanical loosening is typically the result of periprosthetic osteolysis, an adverse biological response to indigestible microscopic wear debris that is resorbed into the bone surrounding the prosthetic joint [9, 10, 11, 12]. The wear debris originates from articulation of the polyethylene liner with the CoCr femoral head by means of adhesive wear, corrosive wear, and/or abrasive wear [13, 14]. Even (highly) cross-linked polyethylene (XL polyethylene), a durable alternative to the commonly used ultra-high molecular weight polyethylene (UHMWPE), while reducing wear [15, 16, 17, 18], has been observed to cause osteolysis [19]. This lack of durability has unacceptable effects, such as riskier revision surgery, re-revision surgery, and surgery postponement that leaves the patient in pain and disability [3, 4]. Therefore, this work aims to reduce the burden of revision surgeries by increasing the longevity of MOP prosthetic hip joints.

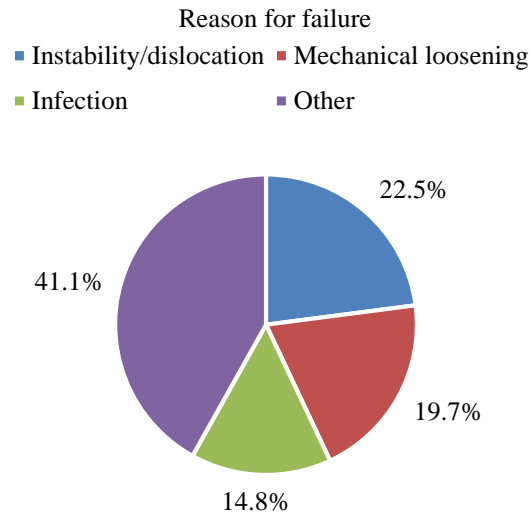


Figure 1.2 Most common reasons for prosthetic hip joint failure. (Data source [8].)

1.2 Terminology

Figure 1.3 depicts a schematic of an MOP prosthetic hip joint, identifying the different components. It consists of a femoral head, usually made of cobalt-chromium (CoCr), which is press-fit or cemented into the femur (thigh bone) through a tapered stem. Stems that are not cemented to the femur typically have a coating that promotes bone growth into the implant, and is often used for patients with high bone quality [20]. The femoral head articulates with a polyethylene liner (usually UHMWPE or more recently XL

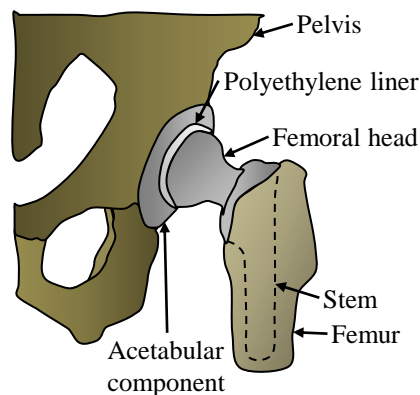


Figure 1.3 Metal-on-polyethylene prosthetic hip joint.

polyethylene and XL polyethylene blended with vitamin E [21]) fixed in an acetabular component that is screwed or cemented to the pelvis [1, 22].

1.3 History

Degenerative joint diseases have been found in ancient human skeletons with a prevalence and distribution little different than it is today [23]. However, little effort was made until the late 1700s when medical knowledge became sufficiently advanced to begin developing extensive surgical practices. Early efforts removed the diseased joint to allow the bone to fuse and immobilize the joint. This procedure was performed as an alternative to amputating the entire appendage. By 1826, surgeons found that “gentle and daily movement” of the joint would fill the cavity with scar tissue and, thus, prevent the bone from fusing, thereby maintaining mobility. However, this approach was “disconcertingly unpredictable” with most joints losing mobility over time despite the extremely perilous procedure [24].

The removal of the diseased joint is still performed today, but subsequent efforts have focused on finding a suitable bearing pair to place in the resulting cavity that replaces the functionality of the original natural joint. Muscle, celluloid, silver plates, rubber struts, magnesium, zinc, glass, pyres, decalcified bone, wax, ivory, pig bladder, and gold foil have been used with limited success [24]. It was not until 1937 when Vitallium®, a metal alloy previously used in dentistry, provided the first “predictable result” in more than 500 patients [24, 25]. By 1964, metal-on-metal (MOM) prosthetic hip joints had provided a “surprisingly good result,” however, its inferior design and poor material selection led MOM prosthetic hip joints to be abandoned in the 1970s in favor of Sir John Charnley’s highly successful MOP prosthetic hips joints [24]. MOM prosthetic hips joints were

reintroduced in the 1980s with improved designs, but questions regarding metal ions resulting from unexpected wear that cause inflammatory reactions, soft tissue necrosis, and osteolysis have limited their success [26, 27, 28]. A third resurgence in the use of MOM prosthetic hip joints started in the early 2000s, with catastrophic consequences, including recalls of implants by most major prosthetic joint manufacturers [29, 30, 31].

Ceramic-on-ceramic (COC), ceramic-on-polyethylene (COP), and ceramic-on-metal (COM) prosthetic hips joints have also been used as an alternative to MOM and MOP joints. COC prosthetic hips joints produce wear debris that is less biologically active than either metal ions or microscopic polyethylene particles, but their brittle nature and their tendency towards edge-loading wear that leads to squeaking have limited their success [23]. COP hip joints have not yet demonstrated a reduction in wear compared to MOP joints [32] and are also more brittle. Additionally, while patients with COM prosthetic joints generally display lower levels of metal ions in their blood stream than patients with MOM joints, early in-vivo failures have limited their success [33, 34]. As a result, MOP prosthetic hip joints presently remain the most popular type of prosthetic hip joint in the United States. Hence, the focus of this work is on MOP prosthetic hip joints.

1.4 Current state of research

The current engineering paradigm for combating implant wear is twofold. First, researchers have attempted to improve the mechanical properties of the polyethylene liner by cross-linking the polymer chains using gamma-irradiation, resulting in XL polyethylene, which has better wear resistance than UHMWPE, but reduced fatigue resistance [15, 16, 17, 18]. Additionally, blending vitamin E in the polymer has improved its oxidation resistance [21]. Second, manufacturing ultra-smooth bearing surfaces, as

witnessed by the re-introduction of MOM [35] and the development of COP [32] and COC prosthetic hip joints [36] has also been attempted to reduce wear of the articulating surfaces. For example, COC articulating surfaces are polished to an average surface roughness $R_a < 5$ nm, which enables them to operate in the (elasto)hydrodynamic lubrication regime, thus reducing friction and wear [37, 38]. Despite this advantage, COC prosthetic hip joints are prone to edge-loading wear that leads to squeaking [39, 40, 41, 42], problems that MOP hips do not exhibit. To date, the potential of reducing friction and wear by increasing the load-carrying capacity of the lubricant film in MOP hips has been neglected, likely because the polymer bearing surface is compliant, prone to dimensional error, and infeasible to polish.

In contrast to the existing knowledge, this work attempts to decrease friction and wear of MOP prosthetic hip joints by adding a patterned microtexture to the ultra-smooth CoCr femoral head, as illustrated in Fig. 1.4. The microtexture is implemented as an array of concave features (“dimples”) and is well known to increase the load-carrying capacity and lubricant film thickness in other man-made bearings [43], such as magnetic tape drives [44, 45], piston rings [46], and thrust bearings [47]. The dimples form microhydrodynamic

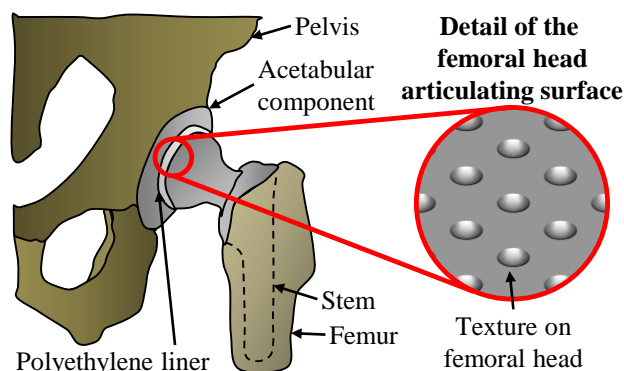


Figure 1.4 Metal-on-polyethylene prosthetic hip joint with a patterned microtexture on the CoCr femoral head. (Reproduce with permission from [48].)

bearings that increase the load-carrying capacity of the lubricant film between two bearing surfaces in relative motion. This increases the lubricant film thickness and reduces contact, thereby reducing friction and potentially reducing wear of the articulating surfaces.

A few researchers have attempted to improve the durability of MOP prosthetic hip joints by using surface texture or by increasing the surface roughness of the femoral head. Ito et al. [49] manufactured circular dimples 0.5 mm in diameter and 0.1 mm deep, with a 1.2 mm pitch on a CoCr femoral head. They observed a 17% reduction in friction and a 36% reduction in polyethylene wear, and hypothesized that this may be the result of the abrasive wear particles being trapped in the dimples and lubricant being accumulated and subsequently dispensed from the dimples during lubricant starvation conditions. Sawano et al. [50] used a waterjet to machine 0.25 μm to 4.4 μm deep channels, spaced 10 μm apart and running perpendicular to the direction of articulation, into a cobalt-chromium-molybdenum (CoCrMo) plate. A modest reduction in polyethylene wear was measured in a pin-on-disc experiment, which was attributed to the channels trapping wear particles. Zhou et al. [51] used a diamond indenter to manufacture spherical dimples of 1 mm in diameter and 2 μm deep into stainless steel plates. They conducted a pin-on-disc experiment with a UHMWPE pin (GUR 1020) and textured stainless steel plates, and concluded that microtexture does not improve lubrication, but instead increased the surface roughness and subsequently wear. However, we observed tall ridges around the contour of the microtexture features, which may have increased friction in the bearing.

Finally, while natural articular cartilage is nominally quite smooth, it has long been known that its surface exhibits a microtexture consisting of shallow grooves and indentations as illustrated in Fig. 1.5 [52, 53, 54, 55, 56, 57], the effects of which,

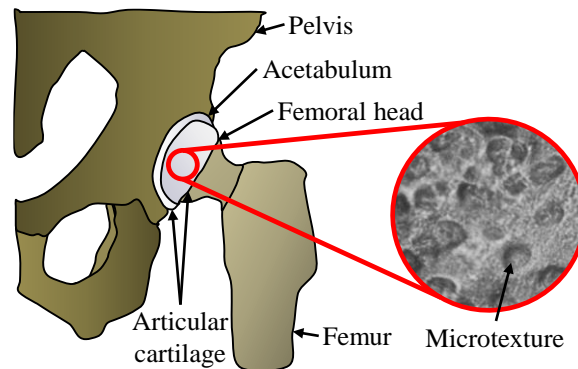


Figure 1.5 Schematic of natural hip joint with the articular cartilage on the femoral head articulating against the articular cartilage in the acetabulum. A magnified view of the surface of articular cartilage is displayed. It shows that the surface of articular cartilage displays many indentations and texture features. The magnified view inset, obtained with reflected light microscopy at a 220x magnification, is from Longmore and Gardner [58]. (Adapted with permission from [59].)

particularly in light of lubrication and longevity, are not fully understood. However, on the basis that surface microtexture improves performance of other man-made bearings, we hypothesize that a patterned microtexture optimized for a prosthetic hip joint will reduce its friction and wear, by means of improved lubrication [59].

1.5 Approach

The engineering objective of this work is to reduce friction, and therefore wear, between the articulating surfaces of prosthetic hip joints by adding a well-defined patterned microtexture to the smooth femoral head, which creates an array of microhydrodynamic bearings that increase the lubricant film thickness. Figure 1.6 illustrates this concept. Asperity contact may occur at the interface between a conventional smooth femoral head and polyethylene liner (Fig. 1.6 (a)). However, when adding microtexture to the smooth femoral head (Fig. 1.6 (b)), the lubricant film thickness is increased, reducing contact and thus also reducing friction and wear.

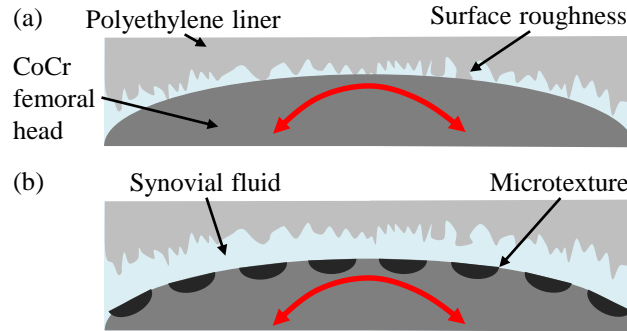


Figure 1.6 Sliding interface between femoral head and acetabular component. The direction of articulation is indicated by red arrows. The average surface roughness of the liner is typically at least one order of magnitude larger than that of the femoral head. (a) Smooth and (b) microtextured femoral head, illustrating that the microtexture increases the thickness of the lubricant film, which reduces asperity contact.

This approach is in stark contrast to the current engineering paradigm of manufacturing smoother articulating surfaces, and differs from earlier research that attempted to use texture as lubricant reservoirs or wear particle traps. A steady-state lubrication model is used to optimize the patterned microtexture geometry in terms of maximum load-carrying capacity or, correspondingly, lubricant film thickness. From these results, four microtexture designs are selected based on maximum load-carrying capacity, and are manufactured on convex CoCr specimens. This work experimentally demonstrates that the friction coefficient between convex CoCr specimens articulating against a concave UHMWPE specimen can be reduced significantly by adding a patterned microtexture to the CoCr specimens.

CHAPTER 2

PATTERNED MICROTTEXTURE DESIGN *

2.1 Model

Figure 2.1 shows a schematic of the lubrication model. The microtextured femoral head is represented by a column of $N = 7$ spherical microtexture features (“dimples”) and moves relative to the smooth acetabular liner. Since the curvatures of the femoral head and acetabular liner are almost identical and much larger than the dimensions of the dimples, the bearing can be approximated as a parallel slider bearing.

The following assumptions are made: (1) each dimple has an identical spherical

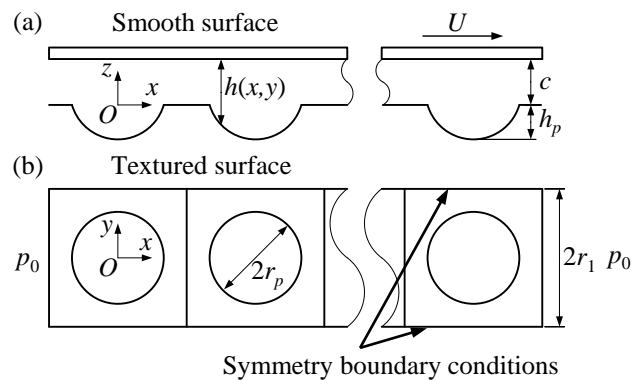


Figure 2.1 Schematic of the lubrication model showing (a) cross-sectional view and (b) top view. (Reproduced with permission from [48].)

* This chapter reports the work of Mingfeng Qiu, a PhD student in the Nanotribology and Precision Engineering Laboratory at the University of Utah. It is a reprint of the material as it appears in Section 2 in [48], and is included in this thesis for completeness and for the justification of how the geometry of the microtexture used in the experiments described in this thesis was selected.

shape and is positioned in the center of a square unit cell of width $2r_1$ (see Fig. 2.1(b)). (2) While it is well-known that synovial fluid is shear-thinning, its shear rate dependence is much smaller in prosthetic joints than in natural joints [60]. Hence, the synovial fluid is modeled as a Newtonian fluid with a viscosity equal to water at room temperature [61, 62], which is a conservative assumption. The viscosity of synovial fluid is typically larger than water, which would increase the hydrodynamic pressure in the model. (3) Inertial forces are neglected because they are at least two orders of magnitude smaller than the viscous forces. (4) The minimum spacing c between the bearing surfaces is sufficient to avoid asperity contact and, thus, hydrodynamic lubrication is maintained assuming abundant lubricant supply. (5) No slip is assumed at the solid boundaries. Thus, the relationship between bearing spacing and pressure is governed by the steady-state two-dimensional incompressible Reynolds equation, given as [63]

$$\frac{\partial}{\partial x} \left(h^3 \frac{\partial p}{\partial x} \right) + \frac{\partial}{\partial y} \left(h^3 \frac{\partial p}{\partial y} \right) = 6\mu U \frac{\partial h}{\partial x}, \quad (1)$$

where x and y are Cartesian coordinates as indicated in Fig. 2.1, $p(x,y)$ is the local bearing pressure, $h(x,y)$ is the local bearing spacing, μ is the dynamic viscosity of the lubricant, and U is the relative sliding velocity between the microtextured and smooth surfaces. Equation (1) can be rewritten in nondimensional form as

$$\frac{\partial}{\partial X} \left(H^3 \frac{\partial P}{\partial X} \right) + \frac{\partial}{\partial Y} \left(H^3 \frac{\partial P}{\partial Y} \right) = \frac{\lambda}{\delta^2} \frac{\partial H}{\partial X}, \quad (2)$$

where $X = x/r_p$, $Y = y/r_p$, $P(X,Y) = p(x,y)/p_0$, $H(X,Y) = h(x,y)/c$. r_p denotes the dimple radius and c is the minimum bearing spacing. The nondimensional flow factor $\lambda = 3\mu U/(2r_p p_0)$

and the nondimensional minimum spacing $\delta = c/(2r_p)$ define the operating conditions of the bearing. The inlet and outlet of the column of N dimples are maintained at ambient pressure p_0 . Symmetric boundary conditions are used on the lateral edges, to mimic the presence of adjacent dimples. Thus,

$$P\left(-\frac{r_1}{r_p}, Y\right) = P\left(\left(N - \frac{1}{2}\right)\frac{2r_1}{r_p}, Y\right) = 1, \quad (3)$$

$$\frac{\partial P}{\partial Y}\left(X, -\frac{r_1}{r_p}\right) = \frac{\partial P}{\partial Y}\left(X, \frac{r_1}{r_p}\right) = 0, \quad (4)$$

with respect to the origin of the coordinate system shown in Fig. 2.1. Reynolds cavitation is implemented to account for gaseous cavitation in the lubricant [63], and the cavitation pressure is assumed to be 90% of the ambient pressure. The patterned microtexture is uniquely described by its texture aspect ratio, $\varepsilon = h_p/(2r_p)$, and texture density, $S_p = \pi r_p^2/(4r_1^2)$. In each dimple cell, the nondimensional local spacing $H(X, Y)$ between the smooth and microtextured surface with spherical dimples is given with respect to a local coordinate system with the origin coincident with the center of the cell as

$$H(X, Y) = \begin{cases} 1, & \text{if } X^2 + Y^2 > 1 \\ 1 + \frac{1}{2\delta} \sqrt{\left(\varepsilon + \frac{1}{4\varepsilon}\right)^2 - (X^2 + Y^2)} - \frac{1}{2\delta} \left(\frac{1}{4\varepsilon} - \varepsilon\right), & \text{if } X^2 + Y^2 \leq 1 \end{cases} \quad (5)$$

2.2 Simulation results

A finite difference approach on a staggered grid [64, 65] with a successive over-relaxation factor of 1.0 to 1.9 is used to solve Eqs. (2), (3), and (4) in conjunction with the

Reynolds cavitation condition, for a range of different microtexture geometries (ε, S_p). The operating conditions $\lambda = 5.94 \times 10^{-4}$ and $\delta = 0.01$ are constants, because the optimal microtexture geometry is almost independent of the operating conditions [66]. Convergence of the numerical solution is obtained when the relative change between two successive iterations of the pressure solution is smaller than 10^{-6} at each grid point. A uniform grid of 301 by 301 nodes per unit cell is selected based on mesh convergence analysis, and further refining the grid does not change the solution by more than 2%. Figure 2.2 shows the nondimensional load-carrying capacity per unit area, $W = (P_{avg} - I)$, as a function of texture density and texture aspect ratio. $P_{avg} = p_{avg}/p_0$ is the average non-dimensional bearing pressure. Four different microtexture designs (ε, S_p) are identified in Fig. 2.2, selected based on maximizing the load-carrying capacity of the bearing or, correspondingly, maximizing the lubricant film thickness.

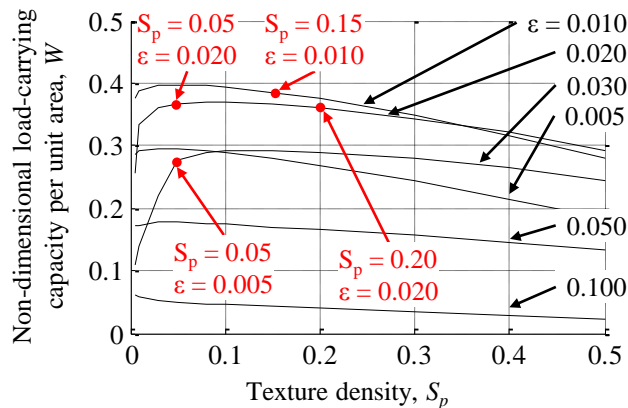


Figure 2.2 Nondimensional load-carrying capacity per unit area as a function of texture density and texture aspect ratio for $\lambda = 5.94 \times 10^{-4}$ and $\delta = 0.01$. The results show that an optimal combination of ε and S_p exists that maximizes the load-carrying capacity or, correspondingly, maximizes the lubricant film thickness. Four patterned microtexture designs are indicated and manufactured on surrogate CoCr femoral heads (see Chapter 4). (Reproduced with permission from [48].)

CHAPTER 3

EXPERIMENTAL APPARATUS *

3.1 Friction and wear tests

3.1.1 Pin-on-disk experiment

A spectrum of different wear testing methods for prosthetic joints exists. Perhaps one of the most simple and affordable methods is the pin-on-disk (POD) experiment. This type of experiment is used to screen different bearing materials rather than testing actual prosthetic joint devices. In a POD experiment, one bearing material is attached to a flat or spherical pin that is loaded against another bearing material affixed to a plate. Friction and wear of the material pair are measured while creating relative motion between the bearing materials.

Several variations of POD experiments for prosthetic joint bearing materials exist as summarized by Gevaert et al. [67]. For instance, a rotary POD experiment consists of a stationary pin loaded against a rotating disk, and a reciprocating POD experiment involves a pin that linearly translates back and forth along the same wear path while loaded against a stationary disk. Since polymer chains in UHMWPE have been found to align with the sliding direction [68, 69, 70], a new class of more sophisticated POD experiments based on multi-axis translation was introduced. The bearing materials are subject to multi-axis

* This chapter is adapted from the material in [98].

shear stresses similar to what occurs in a hip joint. For instance, in a circularly translating POD experiment, a stationary pin is loaded against a disk that translates in a circular pattern without rotation. Additionally, multi-axis POD experiments based on the traditional reciprocating POD experiment exist as well, but include additional degrees of freedom. Important distinctions in the latter method include multi-directional [71, 72], change path [73] and cross-path [73, 74, 75] wear tracks.

While it is desirable to reduce the complexity of hip kinematics and loading when performing initial screening of bearing materials, the simple POD experiments are often performed under conditions that have limited clinical relevance to the in-vivo application [70, 76, 77]. Hence, to simulate in-vivo wear of bearing materials, sophisticated artificial joint simulators are employed to perform wear testing under simulated gait, and to obtain clinically relevant results.

3.1.2 Prosthetic hip joint simulator

Prosthetic hip joint simulators can account for the six degrees of freedom in the hip joint [78] and the corresponding forces and moments. The six degrees of freedom include the anterior/posterior (AP), medial/lateral (ML) and proximal/distal (PD, axial – along femur) translations; and flexion/extension (FE), internal/external (IE), and abduction/adduction (AA) rotations – as shown in Fig. 3.1 [79, 80]. However, the most important kinematic component for friction and wear testing is the FE rotation, which spans 25° to -18° [80]. Large muscles produce large joint reaction forces in a prosthetic hip joint, and loading varies during normal walking gait between approximately 0.3 kN and 3.0 kN in the axial direction [80, 81, 82] for a person weighing approximately 100 kg. The resulting maximum contact stress between the femoral component and the polyethylene

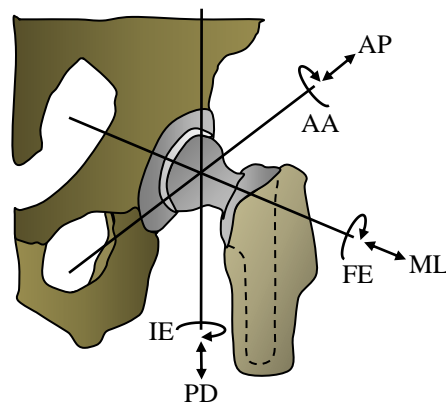


Figure 3.1 Six degrees of freedom of the prosthetic hip joint: AP, ML, and PD translations and FE, IE, and AA rotations. The acetabular component is fixed in space with the femoral head in relative motion. (Data source [79, 80].)

acetabular liner, which can be calculated using Hertz theory [83], is close to 12 MPa [84].

However, nominal contact stresses ranges from 0.5 to 1.0 MPa [84].

Creating these forces in a prosthetic hip joint simulator is achieved by actuating them as forces in force-control hip simulators, or by reproducing the expected motions from the forces in displacement-control hip simulators [85]. The earliest prosthetic hip joint simulators only included flexion/extension and axial loading [86]. Dowson et al. [87] designed the first simulator to specifically measure prosthetic hip joint wear. Axial and AP forces were applied hydraulically, synchronized with the FE rotation. Distilled water was used as a lubricant. Pappas et al. [88, 89] included FE and IE rotation, AP translation, and axial compressive loading in their simulator design, motivated by the need to test mobile bearings. Furthermore, the Durham [90] and Stanmore [91] simulators provided multistation force-controlled wear testing according to the ISO 14243-1 standard [92], while the AMTI, Shore Western [93], and ProSim simulators [94] enabled displacement-controlled wear testing according to ISO 14243-3 [95].

3.1.3 Hybrid experimental apparatus

The use of prosthetic hip joint simulators is time consuming and costly. At least five million gait cycles must be simulated to obtain clinically meaningful data. In addition, the gait cycle frequency is typically limited to 1 Hz and does not exceed 1.5 – 2.0 Hz. Hence, such a prosthetic hip joint simulator experiment lasts 3 – 9 months [85] and, thus, it cannot be used for testing a vast number of different designs and bearing material pairs. On the other hand, POD experiments are fast and efficient, but the testing conditions and environment are sometimes remote from the in-vivo application one attempts to replicate. An accelerated friction and wear test that is inexpensive and fast, yet still provides an environment relevant to the in-vivo application is needed to enable screening of large sets of bearing material pairs, prior to testing a select number of materials and designs in a prosthetic hip joint simulator.

Additionally, friction forces between the articulating bearing surfaces are not generally measured in the aforementioned POD and prosthetic hip simulator devices. However, monitoring friction could yield important information about the inception and evolution of contact and wear of the bearing surfaces, and it enables monitoring the transition between boundary and (elasto)hydrodynamic lubrication. Hence, the objective of this chapter is to describe the design of a hybrid apparatus that combines aspects of both the POD and hip simulator and enables measurement of friction and wear to enable efficient durability screening of prosthetic hip joint bearing materials prior to simulator testing.

3.2 Concept

Figure 3.2 illustrates the concept of the experimental apparatus. A cylindrical specimen (surface 1), representing the femoral component of the prosthetic hip joint, is mounted on a horizontal shaft that rotates reciprocally, representing FE rotation. A mating specimen (surface 2) representing the acetabular liner is loaded perpendicular to the rotation axis of the cylindrical specimen, mimicking dynamic axial loading. The magnitude of the normal load is synchronized with the angular position of the shaft to mimic a hip gait cycle. The torque M_t to rotate the shaft and the normal load N acting on the articulating surfaces are measured, and the friction coefficient as a function of time is computed from these measurements. The entire articulating surface is submerged in a reservoir filled with lubricant (typically, bovine serum with protein concentration of 30 mg/ml to simulate joint fluid [96]) and, thus, traditional gravimetric wear measurements with or without soak controls can be performed to supplement the friction measurements [97].

Different contact scenarios from cylindrical on flat (Fig. 3.2(a)) to fully conformal convex and concave cylindrical (Fig. 3.2(c)), and any contact geometry in between (Fig. 3.2(b)) can be implemented. The apparatus is a significant simplification of a hip simulator and is more sophisticated than a POD experiment. It mimics FE rotation synchronized with

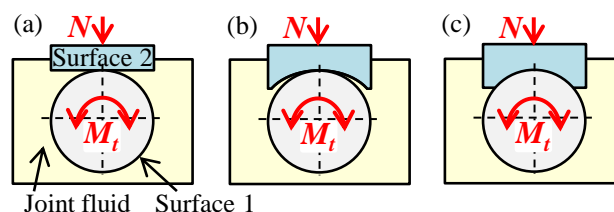


Figure 3.2 Concept of the apparatus, showing two articulating prosthetic hip joint bearing surfaces subject to a torque moment M_t and normal load for N (a) cylindrical on flat, (b) convex cylindrical on concave cylindrical, and (c) fully conformal contact. (Reproduced with permission from [98]).

dynamic axial loading but neglects the AP and ML translations and the IE and AA rotations, i.e., the apparatus only simulates sliding and no cross-shear can be created. The simplifications are implemented because this apparatus is geared towards measuring friction between the bearing surfaces of surrogate prosthetic hip joint components, and studying the effects of (elasto)hydrodynamic lubrication induced during articulation. Friction is an early indicator of wear and, thus, an important parameter when performing short-duration wear tests.

Since a majority of the relative motion in a prosthetic hip joint is uniaxial resulting from FE rotation, it seems desirable to measure friction in a uniaxial sliding test. Thus, the time-evolution of friction can be monitored throughout the entire imposed kinematic cycle. This is particularly important during changes in sliding direction when the bearing may transition between boundary, mixed, and (elasto)hydrodynamic lubrication. Direct measurement of the friction coefficient in addition to traditional wear measurement is not possible in most hip simulators. This apparatus is also more economical and faster than a hip simulator for screening bearing material pairs.

3.3 Mechanical design

The mechanical assembly of the apparatus consists of three parts: the FE rotation drive mechanism, the dynamic loading mechanism, and the base structure with lubricant reservoir. Figure 3.3 shows a schematic of the apparatus, and Fig. 3.4 shows the implementation of this design. The FE mechanism consists of a reciprocally rotating shaft driven by a stepper motor with a 10:1 gear reduction to increase torque. The gearbox is connected to the shaft via a helical coupling (which absorbs misalignment in the drive mechanism) and an in-line torque sensor. The shaft is supported in two bearings mounted

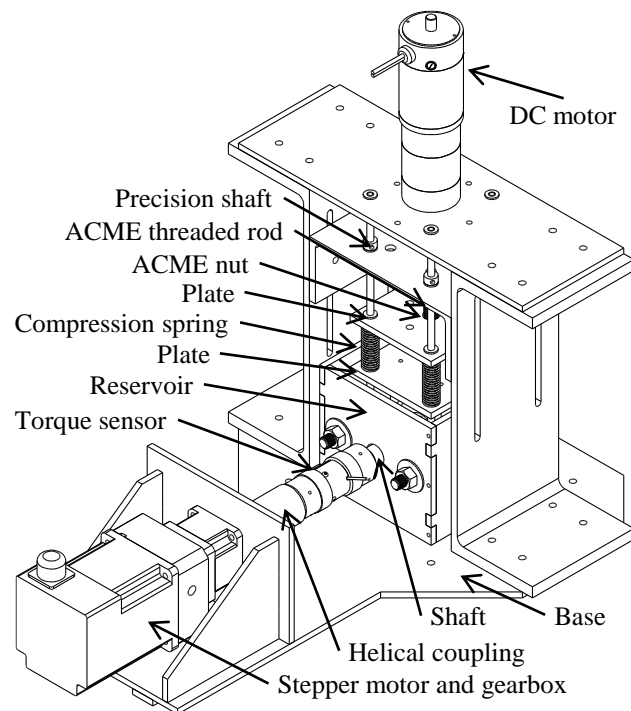


Figure 3.3 Mechanical design of the experimental apparatus. (Reproduced with permission from [98]).

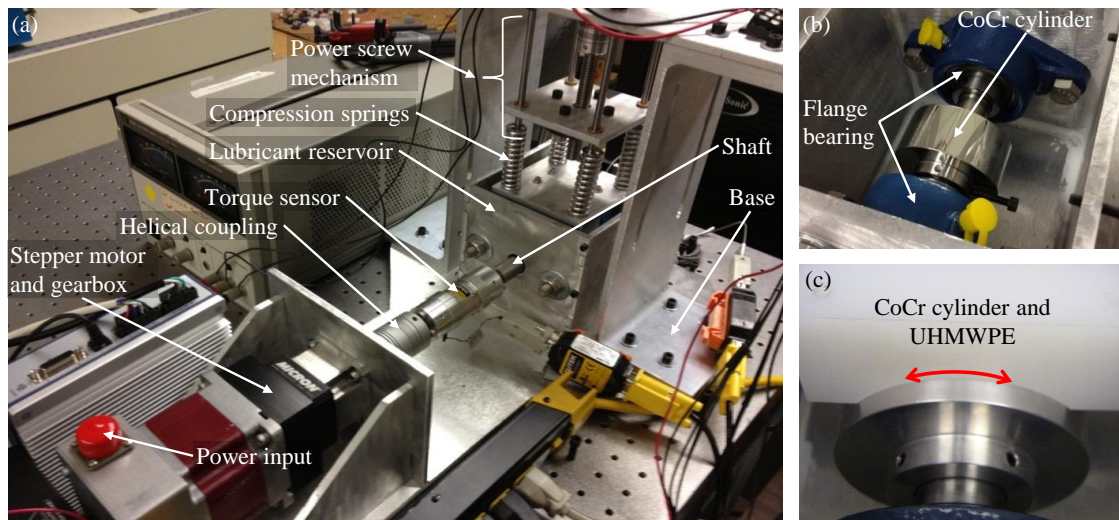


Figure 3.4 Implementation of the experimental apparatus (a) overview picture, (b) detail of the cylindrical CoCr cylinder mounted on the reciprocating shaft in the reservoir, and (c) detail of the interacting CoCr and UHMWPE articulating surfaces. (Reproduced with permission from [98]).

on the inside of the lubricant reservoir sidewalls as depicted in Fig. 3.3(b). A cylindrical specimen (surface 1) is mounted on the shaft in the reservoir by means of four set-screws. It is centered with respect to the shaft rotation axis using a temporarily positioned dial indicator (not pictured). A rubber seal between the bearing housing and the lubricant reservoir wall prevents joint fluid leakage.

The normal loading mechanism is illustrated in Fig. 3.5 and works as follows. Four precision shafts, anchored in the frame of the apparatus, are guided through brass bushings in two separate square plates. One plate holds an ACME nut and is driven up and down the precision shafts by a DC motor, which is mounted on the frame of the apparatus and rotates an ACME threaded rod through its ACME nut (power screw). The second plate serves as a specimen holder for surface 2 and has a load cell embedded in it to measure the normal load. Four compression springs separate the two square plates. These springs are compressed when the plate that seats the ACME nut is driven towards the specimen holder, thus loading the articulating surfaces. The normal load is synchronized with the angular

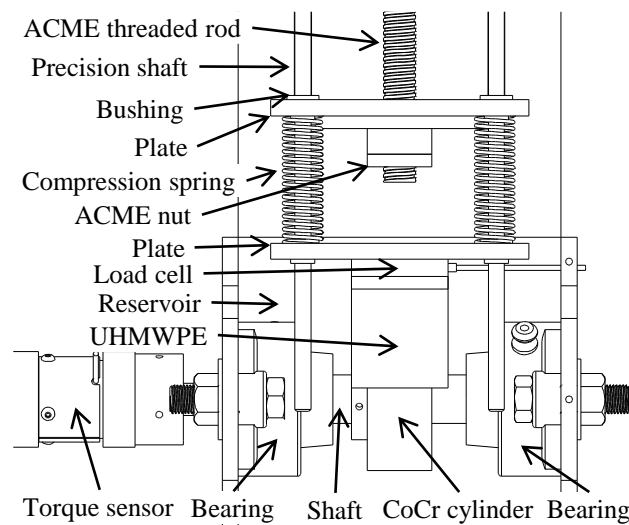


Figure 3.5 Detail of the load mechanism, showing the threaded rod and ACME nut, as well as the precision shafts with compression springs that create the load. (Reproduced with permission from [98].)

position of the cylindrical specimen (surface 1), and it varies with time to replicate the axial the articulating bearing specimens. The only misalignment results from manufacturing the articulating bearing specimens. The only misalignment results from manufacturing tolerances of the convex/concave bearing surfaces. The base frame provides alignment of the different components that constitute the apparatus and affords rigidity to the entire assembly. Furthermore, the lubricant reservoir is integrated in the base structure and allows regulating the amount of lubricant supplied to the bearing interface by means of regulating the lubricant level in the reservoir.

3.4 Specimen design

Any axis-symmetric specimen (surface 1) can be mounted on the reciprocating shaft. The contour of the second test specimen (surface 2) is computed such that a prescribed contact area is obtained when loaded against bearing surface 1. Sanders and Brannon [99] demonstrated that any arbitrary Hertzian contact pair can be substituted by another surrogate contact pair that replicates the contact area and contact pressure distribution of the original contact pair to second-order accuracy. Hence, the complex contact between the femoral head and the acetabular liner can be replaced by a much simpler contact pair, for instance the combination of a circular cylinder or a flat surface and an ellipsoid. In one dimension, the equivalent radius of curvature R_{eq} of two curved surfaces with radius of curvature R_1 and R_2 , respectively, is given as [100]

$$\frac{1}{R_{eq}} = \frac{1}{R_1} + \frac{1}{R_2}. \quad (6)$$

Thus, the elastic contact of a bearing material pair with radius of curvature R_1 and

R_2 can be replaced by a specimen with radius of curvature R_{eq} in contact with a flat one. The surface roughness of each specimen is controlled to match that of actual commercial prosthetic hip joints. Figure 3.6 shows typical specimens used in this apparatus. Figure 3.6(a) shows a CoCr cylinder of diameter 50 mm and width 25 mm (surface 1), finished to a surface finish of $R_a = 50$ nm. The section with reduced diameter seats four set-screws for mounting on the reciprocating shaft. Figure 3.6(b) displays two possible UHMWPE shapes for surface 2; a flat surface that together with surface 1 results in curved on flat contact (as in Fig. 3.2(a)), and a curved surface that results in convex on concave contact (as in Fig. 3.2(b) and (c)). The polyethylene parts are finished to $R_a = 500$ nm.

3.5 Instrumentation

Figure 3.7 shows a schematic of the instrumentation of the experimental apparatus. It consists of separate sections that handle the FE rotation drive mechanism, the normal load mechanism, and the input/output of data. A computer reads an input file that contains the axial bearing load as a function of time throughout the hip gait cycle. This bearing load is synchronized with the angular position of the stepper motor using an open loop

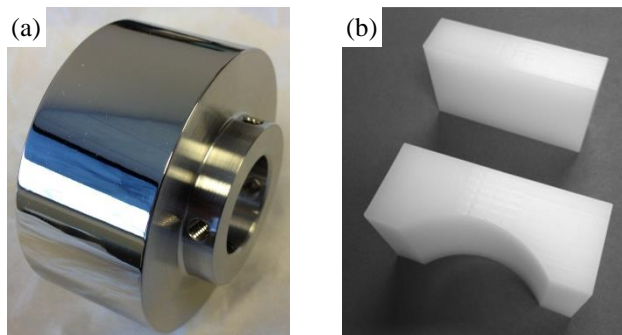


Figure 3.6 Typical examples of bearing pair specimens, showing (a) CoCr cylindrical surface 1, mounted on reciprocating shaft and (b) UHMWPE surface 2 mounted on the loading mechanism. (Reproduced with permission from [98].)

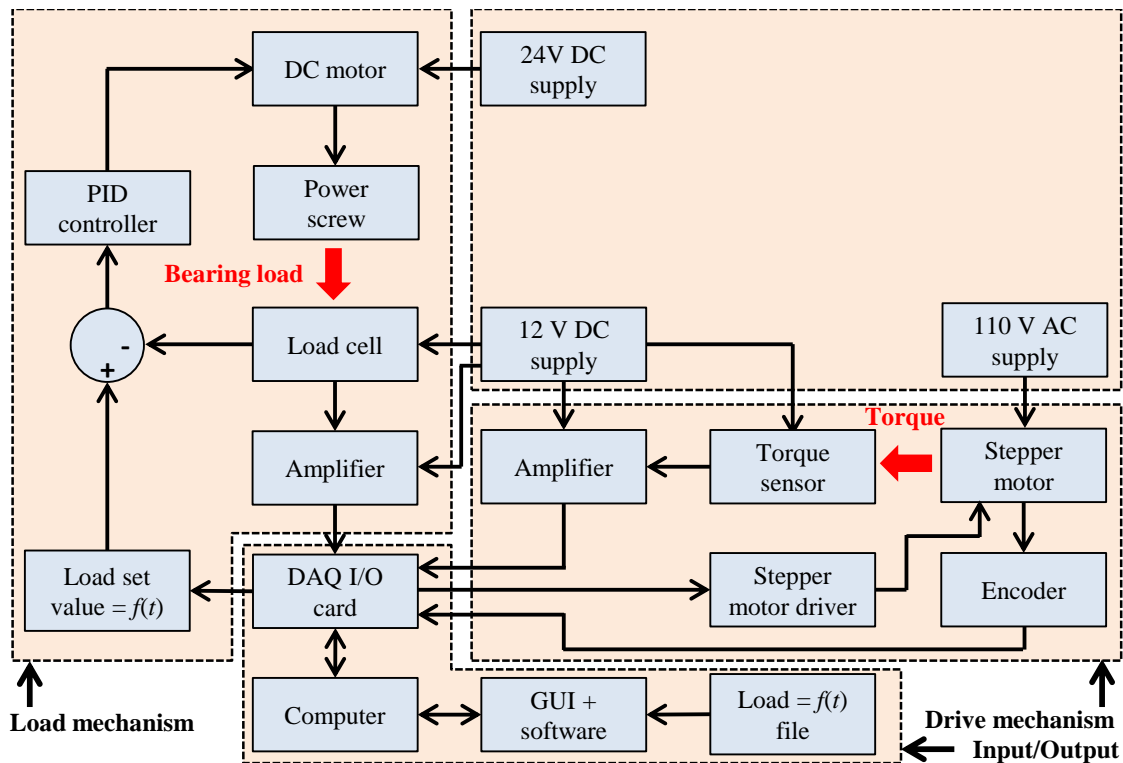


Figure 3.7 Instrumentation of the normal load mechanism, FE rotation drive mechanism, and data input/output. (Reproduced with permission from [98].)

controller. The required normal bearing load is the input to the controller of the DC motor driving the power screw that loads the articulating surfaces. A load cell (Futek LTH300) measures the normal load and closes a force control loop that adjusts this load as a function of time. Furthermore, the stepper motor rotates reciprocally, controlled by a stepper motor driver, and the torque to rotate the shaft is measured by a torque sensor (Futek TTF350). Both load cell and torque sensor signals are amplified (Futek CSG110) and then digitized using a data acquisition (DAQ) card (Sensoray 626). Continuous measurement of the normal load and the torque enables computing the friction coefficient as a function of time, an important indicator of expected wear.

3.6 Friction measurements

While practically any load and sliding velocity as a function of time sequence can be implemented in this apparatus, the ISO 14242-1 standard prescribes the loading and displacement during gait for friction and wear testing of prosthetic hip joints [80]. The friction coefficient is calculated from the continuous normal load and torque measurement during a friction experiment. Wear measurements may be performed using the traditional gravimetric technique based on weight loss of the polyethylene part as a result of wear, with or without soak control [85, 101]. White light interferometry of the worn surfaces can be used as well to obtain an estimate of the wear volume of the specimen. The latter technique, while quick, is known to cause error by neglecting the deformation created by creep [85, 102].

The lubricant reservoir has a volume of approximately 1.5 liter and is filled with joint fluid for durability wear testing. The composition of the joint fluid affects the results of a durability wear test; see for instance [96, 103, 104]. The ISO 14242-1 standard [80] prescribes a protein concentration of 30 mg/ml, a value that is often reported in the literature and appears to represent a consensus among wear test practitioners.

Figures 3.8 and 3.9 show results obtained for the specimens depicted in Fig. 3.6, i.e., a convex CoCr cylinder in conformal contact with a concave (contact span of 90°) and flat UHMWPE specimen, respectively. The contact geometry of an actual prosthetic hip joint falls in between convex-concave conformal contact, and convex on flat contact. Both Figs. 3.8 and 3.9 show (a) the kinematic cycle, characterized by velocity and angular position of the convex cylinder with respect to the stationary polyethylene specimen, (b) the normal load, (c) the torque normalized with the maximum torque, and (d) the friction

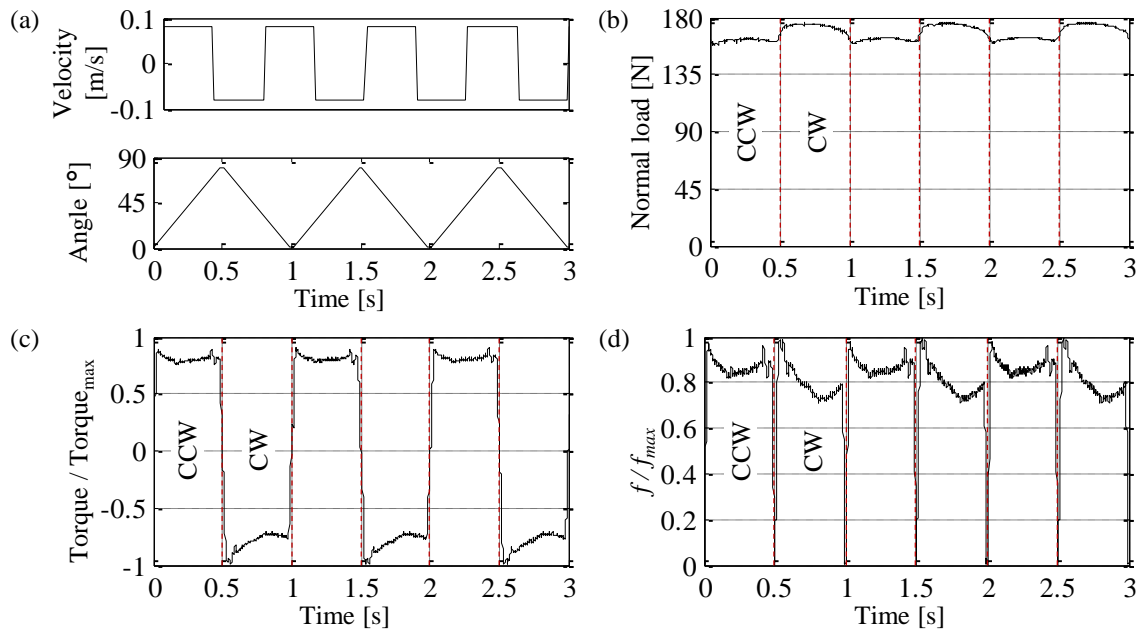


Figure 3.8 Typical friction measurement of a convex CoCr cylinder articulating against a conformal concave UHMWPE specimen (contact span is 90°), (a) kinematic input cycle, (b) normal load, (c) normalized torque, and (d) normalized friction coefficient, as a function of time. (Reproduced with permission from [98].)

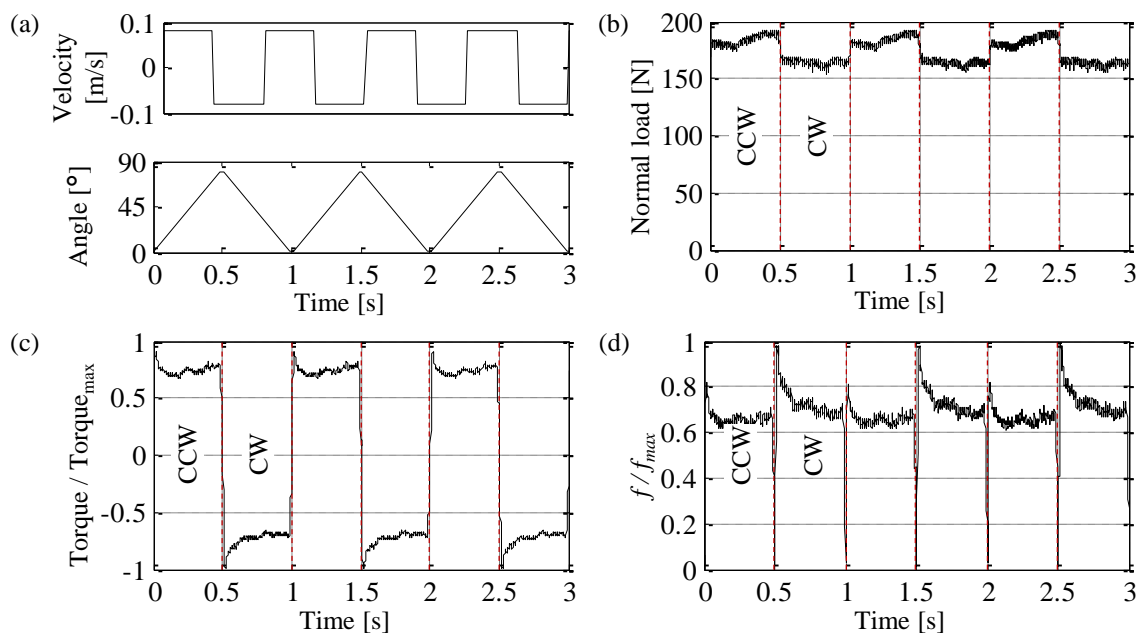


Figure 3.9 Typical friction measurement of a convex CoCr cylinder articulating against a flat UHMWPE specimen, (a) kinematic input cycle, (b) normal load, (c) normalized torque, and (d) normalized friction coefficient, as a function of time. (Reproduced with permission from [98].)

coefficient f normalized with the maximum friction coefficient f_{max} . Three seconds extracted from a long duration measurement performed with this apparatus are presented. Using Hertz contact theory, the normal loading results in a maximum contact pressure of 9.4 MPa and 1.1 MPa for the flat and conformal UHMWPE specimen, respectively. These values are realistic for part of the gait cycle during walking on flat ground for in-vivo prosthetic devices [84]. The sliding direction is indicated as counter-clockwise (CCW) and clockwise (CW), and the gait cycle frequency is 1 Hz. The friction coefficient varies dynamically and is periodic with reversals between CCW and CW rotation. Moreover, the magnitude variation during each period can be interpreted to identify the different phases of the kinematic input cycle. For example, f/f_{max} is maximal at the starts and stops, and it is minimal in the middle of each cycle, corresponding to constant-speed rotation and sliding (0.1 m/s) realistic for in-vivo prosthetic hip joints [80]. Also, the friction coefficient is found to increase with increments of normal load, as expected (not shown) [100]. Note that the variation in normal load is due to slight eccentricity of the convex CoCr specimen.

3.7 Limitations

An important aspect of this newly developed apparatus is that it provides a method for performing fundamental friction and wear tests in a more clinically realistic context than what is provided by other screening wear test experiments such as POD apparatuses. While this apparatus neglects AP and ML translation as well as IE and AA rotation investigated by other authors, the hydrodynamic wedge effect, which can strongly influence friction and wear, can be simulated by designing the bearing surfaces as in Fig. 3.2(b). Thus, a multitude of (elasto)hydrodynamic conditions using differently shaped polyethylene components can be evaluated. This same effect cannot be induced using the

flat-on-flat surface configuration of the ASTM standard POD wear test [105], much less to represent any particular design of a hip bearing pair. Also, the possibility to vary the normal loading as a function of time, synchronized with the angular position of the CoCr cylinder enables changing the contact stress in a single gait cycle, while measuring the bearing friction coefficient. With this new system, no actual, finished prosthetic hip joints are required, yet the contact mechanics of a specific contact pair can still be accurately simulated by means of a simplified surrogate contact pair that creates the same contact area and contact pressure as the actual bearing pair [99]. Indeed, the simplified surrogate pair is easier to manufacture, and, thus, it is suggested that a principal benefit of the new system is for measuring the friction and wear of prospective designs rather than finished designs – to optimize them before they enter the lengthy stages of manufacturing development, whereupon it becomes quite difficult for manufacturers to enact further important design changes.

The new apparatus also enables evaluating the effect of clearance between the two components of a prosthetic hip joint on the friction coefficient during a gait cycle, as well as wear after many cycles. Furthermore, it is significantly more sophisticated than most POD experiments because it can simulate dynamic axial loading and FE rotation; yet, the expense and difficulty of performing experiments with this new apparatus is similar to that of POD experiments and much less expensive than complicated simulator testing. Multistation testing can also easily be implemented.

Doubt exists about the clinical relevance of friction and wear data obtained with POD experiments. Clinically relevant data must be obtained with hip simulators. The value of this apparatus lies in that it allows fast and inexpensive friction testing of prosthetic hip

joint bearing materials with boundary conditions that are more clinically relevant than those of a POD apparatus. This device could benefit from an additional degree of freedom, such as IE or AA rotation. This would add cross-shear to the wear testing, which has been demonstrated to increase wear by avoiding alignment of polyethylene fibrils. However, these additional degrees of freedom are much smaller than the sliding resulting from FE rotation. Hence, many prosthetic hip joint wear experiments neglect these additional degrees of freedom.

CHAPTER 4

SPECIMENS *

4.1 Manufacturing process

Several manufacturing techniques have been used to create a well-defined patterned microtexture on engineering surfaces, which include: vibro-rolling for the fabrication of undulated surfaces [106], reactive ion etching [107], abrasive jet machining [108, 50], lithography and anisotropic etching [109, 49], lithography electroplating and molding (LIGA) [110], indentation [51], and vibro-mechanical texturing [111]. However, laser surface texturing (LST) appears to be the most commonly used technique [112, 113, 114, 115, 116], in particular for its excellent control of the microtexture geometry and its short processing time, which together allows quick implementation of prototype designs [43]. Figure 4.1 shows a schematic of the LST process. A laser beam (typically Nd:YAG) is focused onto the surface of a smooth CoCr (ASTM F1537-08) cylinder used as a surrogate femoral head. During each pulse, the surface of the CoCr cylinder is locally ablated as the material transitions directly from a solid to a gas, which creates the dimple-like microtexture. Bulges may form around the dimple as a result of ablated particulate condensing. These bulges are considered to be a manufacturing defect, because the bulges may create abrasive wear when the CoCr cylinder articulates with the polyethylene

* This chapter is adapted from the material in [48].

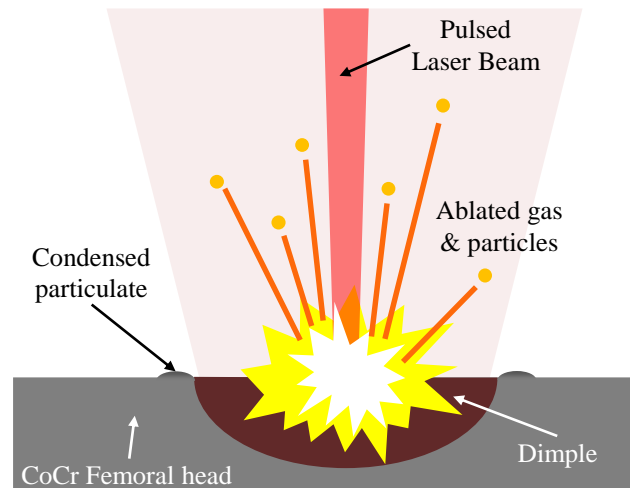


Figure 4.1 Laser surface texturing process. A pulsed laser beam is focused onto the surface of CoCr femoral head, and ablates the surface, creating a dimple-like texture feature.

specimen. The sizes of these bulges around the texture features is minimized by controlling the pulse duration, energy per pulse, laser spot size, and surrounding airflow. Each of the cylinders has a diameter of 50 mm and are machined, lapped, and polished to $R_a < 50$ nm before LST. The dimple radius $r_p = 50$ μm for the four microtexture designs identified on page 12.

4.2 Characterization

The surface roughness of all specimens is characterized using standard optical microscopy and white light interferometry (WLI). WLI is a noncontact optical method to measure surface topography. A collimated broadband light source is passed through a beam splitter where half the light travels to the test surface and the other half to a smooth reference mirror. The light reflected from the test specimen and the reference mirror is recombined and superimposed onto an image sensor. The superimposed images form interference patterns from which the surface topography can be computed [117, 118].

Creating an image of the surface roughness within the dimples is very difficult.

First, the light absorptivity of the area within the dimple is much higher than that of the surrounding land area, and to prevent the land area in between the dimples from becoming oversaturated while the area within the dimple is imaged, each microtexture pattern is imaged twice under different lighting conditions with the subsequent images stitched together using MetroPro, a commercial software program used to visualize data from the white light interferometer (Zygo NewView 5032). Areas that could not be imaged, i.e., the dimple side walls, are filled with interpolated values using the surrounding data from areas that could be imaged, which is a common and accepted procedure that is automated by the MetroPro software. Second, the high frequency roughness within the dimples creates an alias that causes large errors within the WLI datasets that must be corrected by postprocessing the raw data. Outlier data points that are larger than two standard deviations from the mean surface roughness inside the dimple are removed and replaced with interpolated values, and a 2-D adaptive Wiener filter using a 7×7 ($2 \mu\text{m} \times 2 \mu\text{m}$) box of nearest neighbors is used to estimate and remove the local noise [119]. This filtering procedure effectively acts as a low-pass filter that digitally polishes the roughness within the dimple, and is used only to allow the overall shape of the dimple to be characterized. Because of the high frequency aliasing, only estimates of the roughness inside the dimple can be obtained.

Figure 4.2 shows optical microscopy and WLI images of each of the four different patterned microtexture designs that are selected from the modeling data discussed in Chapter 2, and manufactured using LST on CoCr cylinders that serve as surrogate femoral heads. A cross-section through the center line of the dimple reveals the surface roughness inside the dimples. Minimal material deposition around the contour of each dimple,

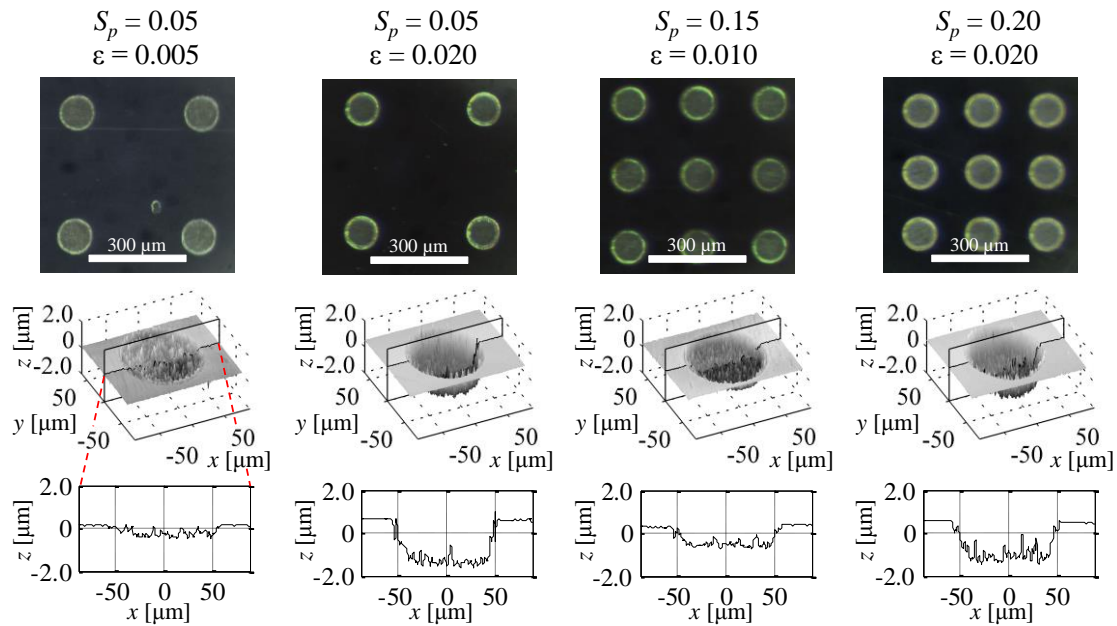


Figure 4.2 Optical microscope and white light interferometer images of each of the four patterned microtexture designs, manufactured on cylindrical CoCr specimens (ASTM F1537-08), showing the results of the LST process. A trace along the centerline of the dimple reveals the surface roughness inside the dimple. The radius of the dimples, $r_p = 50 \mu\text{m}$. The texture parameters S_p and ε are defined on page 12. (Reproduced with permission from [48].)

resulting from the LST process, is observed. The land area between the dimples is extremely smooth ($R_a = 12 \text{ nm}$) and identical to the untextured benchmark. However, within the dimple the roughness can be as high as $R_a = 350 \text{ nm}$. It is also noted that the roughness inside the dimple poses a practical limit for the minimum dimple depth that can be achieved with LST. From Fig. 4.2, we observe that the magnitude of the surface roughness is on the same order of magnitude as the actual dimple depth, for the case of $\varepsilon = 0.05$ (dimple depth is $0.5 \mu\text{m}$, surface roughness $R_a = 350 \text{ nm}$).

Figure 4.3(a) and (b) show a photograph and a flattened white light interferometry image, respectively, of a smooth cylindrical CoCr specimen used as a benchmark in the friction experiments. Figure 4.4 depicts the concave UHMWPE (GUR 1020-ASTM F648) specimen of diameter 50.75 mm , machined by Orchid Orthopedics to $R_a = 500 \text{ nm}$. The

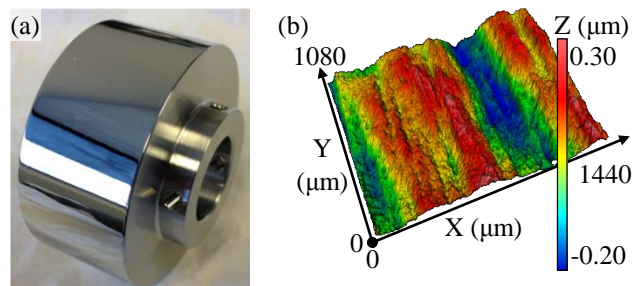


Figure 4.3 Smooth cylindrical CoCr specimen (a) photograph and (b) white light interferometer image of the articulating surface. (Reproduced with permission from [48].)

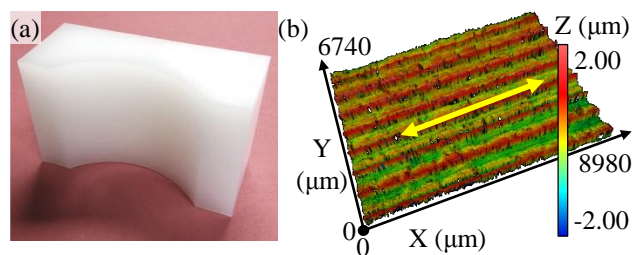


Figure 4.4 UHMWPE specimen (a) photograph and (b) white light interferometer image of the articulating surface. The yellow arrow indicates the direction of articulation. (Reproduced with permission from [48].)

cylinder profiles are subtracted in the WLI images to allow quantifying the surface topography. Both the CoCr and UHMWPE specimens are manufactured and finished to identical surface topography specifications as commercial MOP prosthetic hip joints. The conformity ratio η between the articulating surfaces is defined as

$$\eta = 1 - \frac{D_i - D_o}{D_o}, \quad (7)$$

where D_o is the outer diameter of the CoCr cylinder, and D_i is the inner diameter of the UHMWPE specimen. $\eta = 98.5\%$ for the specimens shown in Fig. 4.3 and 4.4. The contact pressure (0.57 – 1.13 MPa) is calculated using Hertz theory and falls within the range of in-vivo values [120, 121].

CHAPTER 5

EXPERIMENTAL METHODOLOGY *

5.1 Example experiment

Figure 5.1 illustrates the experimental methodology. Figure 5.1(a) shows the imposed kinematic cycle including velocity and angular position of the CoCr cylinder with respect to the concave UHMWPE counterface as a function of time. The kinematic cycle is designed to maximize the portion during which a constant sliding velocity is maintained, to best approach the steady-state lubrication model used to optimize the microtexture geometry. The frequency of the kinematic cycle is 1.0 Hz [122] (ISO 14242-1), similar to a walking gait. Figure 5.1(b) shows the friction coefficient f as a function of time for the textured ($S_p = 0.05$, $\varepsilon = 0.005$) and smooth CoCr cylinders, respectively, articulating with the UHMWPE specimen. Only two seconds of data are shown, extracted from a long-duration experiment, to illustrate the detailed measurement of the friction coefficient as a function of time. The normal load, which is held constant for comparison to the steady-state lubrication model, is selected to create a maximum contact pressure similar to that experienced in in-vivo prosthetic hip joints during walking on flat ground [84]. The maximum contact pressure between the CoCr cylinder and the UHMWPE specimen in the experiment shown in Fig. 5.1 is 0.71 MPa, calculated using Hertz contact theory [83].

* This chapter is adapted from the material in [48].

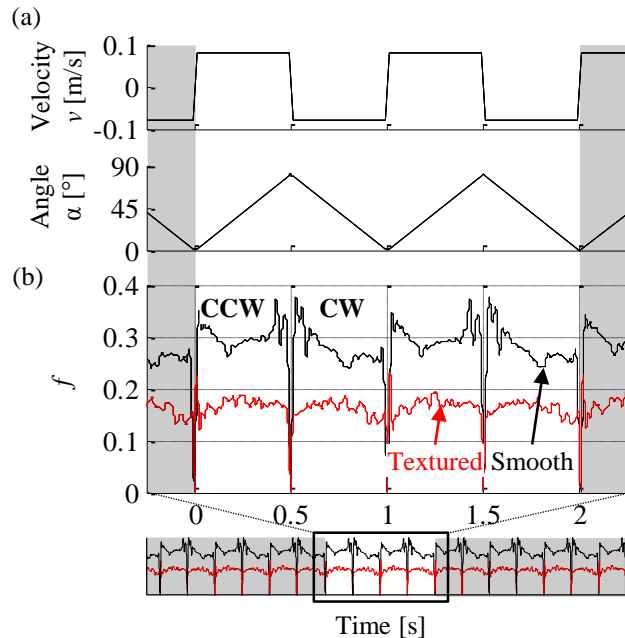


Figure 5.1 Typical experiment showing input kinematic cycle and output friction coefficient as a function of time. (a) Kinematic cycle of the CoCr specimen articulating with the UHMWPE specimen. (b) Friction coefficient as a function of time for the microtextured (red) specimen ($S_p = 0.05$, $\varepsilon = 0.005$) and the smooth (black) specimen, showing that the microtextured specimen outperforms (as quantified later in Chapter 6) the smooth specimen over almost the entire kinematic cycle. (Reproduced with permission from [48].)

5.2 Repeatability and reliability of the experiments

Quality control is implemented to ensure the reliability and repeatability of the experimental results. The following procedures are followed.

- The effect of the viscoelasticity of the UHMWPE sample is controlled by allowing the experiment to reach steady-state where one kinematic cycle is indistinguishable from the next, prior to making a friction measurement.
- The lubricant temperature is recorded at the start and end of each experiment for record keeping purposes since the viscosity is a strong function of temperature. The lubricant temperature is room temperature, 23 °C.
- The lubricant is not reused between experiments to prevent wear particles being

suspended in the lubricant, and the CoCr specimen and UHMWPE specimens are thoroughly cleaned at the start of each experiment to prevent them from carrying potential third-body wear particles into the apparatus that may affect the results.

- Each component of the apparatus is marked in order to ensure that the apparatus is assembled in the same order with the same orientation for each part for each experiment. Additionally, alignment of the components of the experimental apparatus is measured using a micrometer gauge.
- Each part is thoroughly cleaned at the end of each day of testing to prevent corrosion that may damage the apparatus.
- The entire normal load assembly is periodically calibrated and is placed into the experiment apparatus as one unit to ensure consistency between experiments. If the normal load assembly is reassembled, the entire unit is recalibrated.

CHAPTER 6




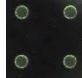
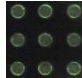
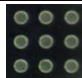
RESULTS AND DISCUSSION *

From Fig. 5.1(b) we observe that the friction coefficient is periodic with reversals between CW and CCW rotations. The friction coefficient is maximum at start and stop ($t = 0.5, 1.0, 1.5$ s), and minimum in the middle of each cycle, when the sliding velocity at the surface of the cylinder is constant (0.1 m/s). The microtextured CoCr specimen outperforms the smooth specimen in two ways. First, the friction coefficient is lower for the microtextured compared to the smooth cylinder over almost the entire kinematic cycle (for this particular microtexture geometry and kinematic cycle example). Hence, this indicates reduced contact between the microtextured CoCr and UHMWPE surfaces compared to smooth articulating surfaces, which can lead to reduced wear. Second, the friction coefficient in the case of the microtextured CoCr cylinder decreases much faster immediately after reversing the sliding direction, compared to the smooth CoCr cylinder. This is indicated by the sharp drop of the friction coefficient surrounding direction reversals (at $t = 0.5, 1.0, 1.5$ s). The patterned microtexture increases the portion of the bearing load that is carried by the fluid, which reduces asperity contact and friction between the articulating surfaces.

Table 6.1 shows the average friction coefficient calculated over a single 1 Hz cycle

* This chapter is adapted from the material in [48].

Table 6.1 Average kinematic friction coefficient for different microtexture designs and contact pressures. The color coding (green – red) is used to visualize the magnitude of the relative values of the friction coefficient. (Adapted with permission from [48].)


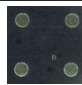
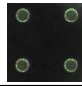
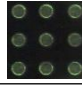
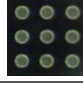
Texture design	Texture parameters	Max contact pressure [MPa]			
		0.57	0.71	0.90	1.13
 300 μm	S_p, ε	0.57	0.71	0.90	1.13
	<i>Smooth</i>	0.26	0.29	0.29	0.28
	$S_p = 0.05,$ $\varepsilon = 0.005$	0.12	0.17	0.23	0.29
	$S_p = 0.05,$ $\varepsilon = 0.020$	0.20	0.26	0.28	0.31
	$S_p = 0.15,$ $\varepsilon = 0.010$	0.19	0.21	0.25	0.29
	$S_p = 0.20,$ $\varepsilon = 0.020$	0.16	0.24	0.25	0.29

extracted from a long duration experiment, for all four patterned microtexture designs articulating with a UHMWPE specimen, and for different values of the contact pressure, ranging between 0.57 – 1.13 MPa. The kinematic cycle is identical to the one shown in Fig. 5.1(a) and the specimens are fully submerged in bovine serum. From Table 6.1 we observe that the average friction coefficient increases with increasing contact pressure, for both smooth and microtextured CoCr cylinders. In all cases, the smooth specimen never outperforms the microtextured ones, except for the cases with contact pressure of 1.13 MPa. The increased load-carrying capacity generated by the patterned microtexture is not sufficient to reduce contact between the articulating bearing surfaces. Thus, solid-on-solid contact occurs between the microtextured CoCr and UHMWPE specimens, which results in a higher friction coefficient than the contact between the smooth CoCr and UHMWPE specimens.

The portion of the kinematic cycle during which each of the microtextured CoCr specimens displays a lower friction coefficient than the smooth CoCr specimen is quantified to evaluate and compare the performance of the four patterned microtexture designs. Table 6.2 summarizes the results and shows the percentage of the kinematic cycle during which the microtextured CoCr cylinder outperforms the smooth one. From Table 6.2 we observe that each microtexture design outperforms the traditional smooth surface over at least part of the kinematic cycle. However, the portion during which the microtextured CoCr cylinder outperforms the smooth one, decreases with increasing contact pressure. This is similar to the results shown in Table 6.1. With increasing contact pressure, the patterned microtexture does not generate enough hydrodynamic pressure to support the increased bearing load and reduce friction between the articulating surfaces.

These results support the hypothesis that friction can be reduced at low sliding

Table 6.2 Different microtexture designs, showing the percentage of the 1 Hz kinematic cycle during which the microtextured CoCr specimen has a lower coefficient of friction than the smooth CoCr specimen, for different values of constant bearing contact pressure. The color coding (green – red) is used to visualize the magnitude of the relative benefit of each microtexture compared to the smooth CoCr specimen. (Adapted with permission from [48].)

Texture design	Texture parameters	Max contact pressure [MPa]			
		0.57	0.71	0.90	1.13
 300 μm	S_p, ε	0.57	0.71	0.90	1.13
	$S_p = 0.05,$ $\varepsilon = 0.005$	98%	98%	94%	24%
	$S_p = 0.05,$ $\varepsilon = 0.020$	88%	67%	58%	19%
	$S_p = 0.15,$ $\varepsilon = 0.010$	94%	96%	91%	22%
	$S_p = 0.20,$ $\varepsilon = 0.020$	93%	90%	83%	15%

velocities in a surrogate MOP prosthetic hip joint by means of a patterned microtexture on the surface of the femoral head. However, at very high contact pressures the hydrodynamic pressure generated by the patterned microtexture may not be large enough to support the bearing load. As a result, contact occurs between the articulating surfaces, and the microtextured CoCr specimen may underperform the smooth one.

The relative performance of the different microtexture designs does not correlate well with the predicted load-carrying capacity (see Fig. 2.2). Several reasons contribute to this observation. First, as pointed out earlier, the manufacturing tolerance of shallow dimples is not held accurately while texturing the entire CoCr specimen, and the magnitude of the surface roughness can be on the same order of magnitude as the desired dimple depth. As a result, the error of the depth of the dimple may be as high as 50% for the microtexture design with $\varepsilon = 0.005$ but decreases with increasing ε . Second, the relative differences in the load-carrying capacity predicted by the model for the four different microtexture designs is small. Thus, minor misalignment of the experimental apparatus, or other external parameters could account for the difference between the experimental and theoretical results. The lubrication model could also be improved by including elastic deformation of the UHMWPE specimen, i.e., using an elastohydrodynamic lubrication (EHL) model instead of a hydrodynamic lubrication model. However, using EHL with a fine numerical grid, needed to resolve the pressure gradients in the dimples, is computationally expensive.

A limitation of the experiments is side-leakage between the articulating cylindrical specimens compared to a ball-in-socket hip prosthesis. Side-leakage is minimal, however, because the unidirectional motion is orthogonal to the sides of the bearing where leakage

occurs. Additionally, it is well known that the boundary effects in textured bearings are limited to the first few rows of dimples adjacent to the boundary. Furthermore, a prosthetic hip joint experiences six degrees of freedom. The most important kinematic component during gait is the flexion/extension (FE) rotation, although other motions create cross-shear in the polyethylene, which markedly affects wear. The experimental apparatus only simulates single-direction FE motion, which limits its scope in investigating the effect of reducing friction. Friction can be an important predictor of wear, and by reducing friction, it indicates the potential of reducing wear in future hip simulator tests that take all degrees of freedom of the prosthetic hip into account.

CHAPTER 7

CONCLUSION *

Based on the numerical and experimental results, we conclude that the friction coefficient between the surrogate convex CoCr and the concave UHMWPE specimens is lower for a microtextured CoCr specimen, than for the benchmark smooth CoCr specimen. The results demonstrate that the patterned microtexture reduces friction by increasing the hydrodynamic pressure and thickness of the lubricant film. This is observed for the four patterned microtexture designs and all values of the contact pressure considered in this study, with the exception of the highest contact pressure used. In that case, the increased load-carrying capacity generated by the patterned microtexture is not sufficient to support the bearing load and reduce friction.

The model-based design of the microtexture geometry is a fast and effective approach to optimize the patterned microtexture geometry, and obtain a range of microtexture parameters that are suitable to reduce friction in the prosthetic hip joint. A reduced friction coefficient between the articulating bearing surfaces promises reduced wear and increased longevity of the prosthetic hip joint. Also, in contrast with the smooth surrogate CoCr femoral head, the friction coefficient decreases very quickly after reversal of the sliding direction for the microtextured surrogate femoral heads. Daily human joint

* This chapter is adapted from the material in [48].

activity includes frequent starts and stops, and it is during these periods of high friction that the most wear occurs. Thus, the microtexture reduces friction and potentially wear precisely at instants where it is most needed.

APPENDIX A

DATA ACQUISITION

An in-house data acquisition (DAQ) application is written in Visual Basic 6.0 and C++ to control the experimental apparatus, and to record the resulting measurements. Figure A.1 illustrates the data recording procedure. Analog voltage signals from the normal and torque load cell are quantized by the Sensoray 626 PCI card. Through a dynamic link library (s626.dll) provided by the manufacturer of Sensoray 626 PCI card, the in-house DAQ application passes a pointer to the memory address of a sixteen element 32-bit integer array to the `S626_ReadADC(int, int[])` function that fills the array with voltage measurements from the load cells. The array of voltage measurements is then copied as a single measurement entry to a large multimeasurement pre-allocated table of time (queried from the system CPU clock), normal loads, and torques. The array of voltage measurements is typically stored in the CPU registers and the large pre-allocated table in RAM for speed. This process is repeated, typically one thousand times a second, until a dataset containing several gait cycles is recorded. The DAQ application then converts the large pre-allocated table from units of CPU clock cycles and quantized volts to units of time (seconds), force (newton), and torque (newton-meter) – that are encoded to an American Standard Code for Information Interchange (ASCII) tab separated value (.tsv)

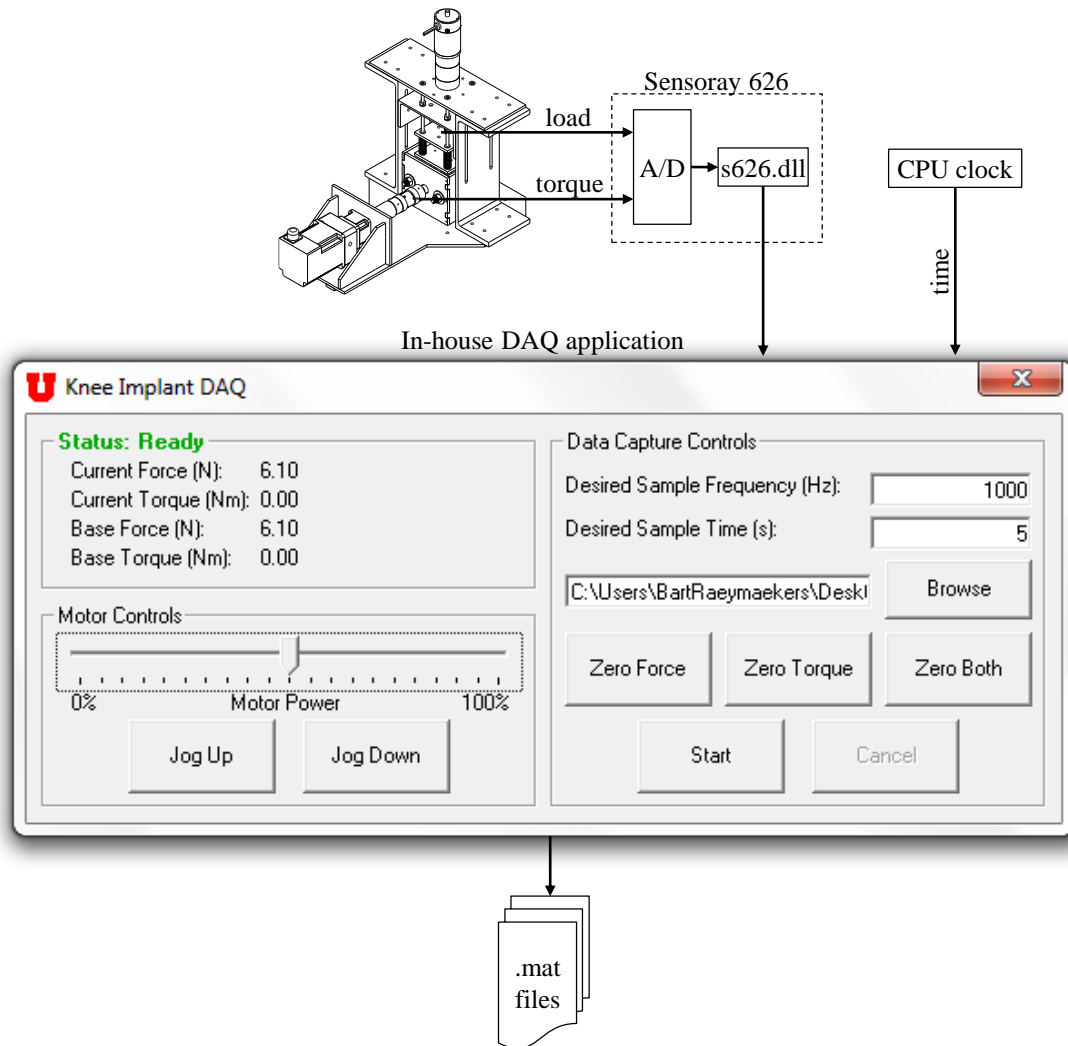


Figure A.1 Schematic of the data recording procedure where analog voltage signals from normal and torque load cells are quantized by the Sensoray 626 PCI card, associated with the time measured by the CPU clock, and electronically archived by an in-house DAQ application.

file on the local hard drive. The ASCII .tsv file is then converted to a .mat file, archived with the dataset's associated meta identifying the experiment parameters, and backed up.

APPENDIX B

DATA REDUCTION

A database containing hundreds of individual datasets of time, normal, and torque for experiments of differing parameters (e.g., lubricant condition, normal load, kinematic cycle, microtexture design, etc.) is processed and mined through a library of MATLAB functions written for this work. Figure B.1 illustrates a typical data reduction procedure. A series of .mat files is loaded into a large heterogeneous structured array with each dataset in its own field space. The dataset's field space is further divided into subfields containing time, normal load, torque, and *meta* (which may be further broken down into sub-subfields identifying the experiment parameters). This hierarchical organization of heterogeneous data allows the hundreds of datasets to be processed and mined by a specific set of rules defined by the user. A typical set of rules is as follows. All datasets are selected and passed through a zero-phase-shift digital low-pass filter (typically a ninth order Butterworth filter that has been digitized and compensated) [123] to remove electrical noise from the normal and torque measurements. It should be noted that the original raw normal load and torque measurements are not overwritten, but the filtered data is appended as an additional subfield within the original dataset's field space. Next, all datasets are selected and passed into series of functions that posttriggers the time such that time equals zero is the point at which the CoCr cylinder first begins to turn counter-clockwise. With all datasets sharing a

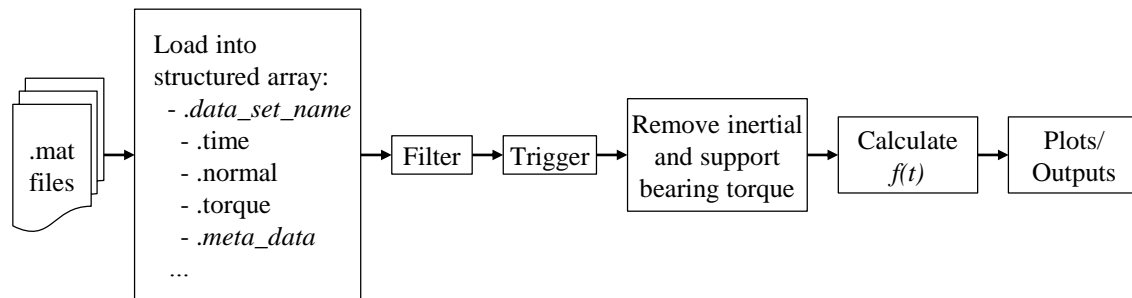


Figure B.1 Schematic of a typical data reduction procedure where the electronically archived datasets are loaded into a structured array in MATLAB, filtered for electrical noise, posttriggered, compensated for inertial and support bearing effects, and displayed.

common time, the inertial and support bearing torque are removed by subtracting the torque of a subset of datasets from the torque of another subset of datasets as shown in Fig. B.2. This allows the subsequent friction calculation to represent the friction between the CoCr cylinders articulating against the UHMWPE specimen only. The filtered, triggered, and compensated datasets are then passed to a series of functions that plot, normalize, and compare the different datasets – an example is Fig. 5.1.

Figure B.2 illustrates the general procedure to remove the inertial and support bearing torque from the dataset. With all datasets having a common time, the datasets

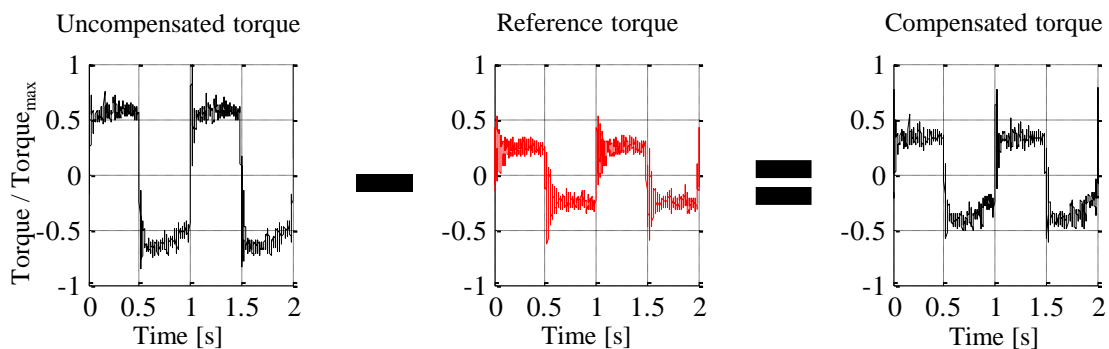


Figure B.2 Detail of the removal procedure for the inertial and support bearing effects. The raw torque for a recorded dataset is subtracted from its zero-normal-load counterpart, thus removing the the inertial and suppor bearing effects.

containing the uncompensated torque are selected from experiments that have a nonzero normal load. The datasets containing the uncompensated torque are then associated with a dataset containing a reference torque through a set of rules using the datasets' meta. The dataset containing the reference torque is defined as the dataset having all experimental parameters the same as the dataset containing the uncompensated torque with the exception of the normal load, which is zero. This torque at zero-normal-load would, thus, represent the inertial and support bearing torque. It should be noted that the inertial and support bearing torque is independent of normal load determined through another experiment.* With the uncompensated torque associated with its reference torque, one is subtracted from the other, as shown in Fig. B.2, resulting in a compensated torque that is used in subsequent calculations.

* The inertial and support bearing torque is found to be independent of normal load through a series of experiments where the CoCr cylinder articulating against a UHMWPE specimen is replaced with a roller bearing articulating against the normal load mechanism. As the normal load increases, the torque remains the same, thus demonstrating that bearing torque is not a function of normal load. Since the inertial torque is a function of angular acceleration only, inertial and support bearing torque is therefore not a function of normal load.

REFERENCES

- [1] American Academy of Orthopaedic Surgeons, "Total Hip Replacement," [Online]. Available: <http://orthoinfo.aaos.org/PDFs/A00377.pdf>. [Accessed 18 May 2014].
- [2] S. Kurtz, K. Ong, E. Lau, F. Mowat and M. Halpern, "Projections of primary and revision hip and knee arthroplasty in the United States from 2005 to 2030," *J. Bone Joint Surg. Am.*, vol. 89, no. 4, pp. 780-785, 2007.
- [3] S. Kurtz, F. Mowat, K. Ong, N. Chan, E. Lau and M. Halpern, "Prevalence of primary and revision total hip and knee arthroplasty in the United States from 1990 through 2002," *J. Bone Joint. Surg. Am.*, vol. 87, no. 7, p. 1487–1497, 2005.
- [4] K. Ong, E. Lau, J. Suggs, S. Kurtz and M. Manley, "Risk of subsequent revision after primary and revision total joint arthroplasty," *Clin. Orthop. Rel. Res.*, vol. 468, no. 11, p. 3070–3076, 2010.
- [5] S. D. Ulrich, T. M. Seyler, D. Bennett, R. E. Delanois, K. J. Saleh, I. Thongtrangan, M. Kuskowski, E. Y. Cheng, P. F. Sharkey, J. Parvizi, J. B. Stiehl and M. A. Mont, "Total hip arthroplasties: What are the reasons for revision?," *Int. Orthop.*, vol. 32, no. 5, pp. 597-604, 2008.
- [6] S. M. Kurtz, *UHMWPE Biomaterials Handbook: Ultra High Molecular Weight Polyethylene in Total Joint Replacement and Medical Devices*, San Diego, CA: Academic Press, 2009.
- [7] S. M. Kurtz, E. Lau, K. Ong, K. Zhao, M. Kelly and K. J. Bozic, "Future young patient demand for primary and revision joint replacement: national projections from 2010 to 2030," *Clin. Orthop. Relat. R.*, vol. 467, no. 10, pp. 2606-2612, 2009.
- [8] K. J. Bozic, S. M. Kurtz, E. Lau, K. Ong, T. P. Vail and D. J. Berry, "The epidemiology of revision total hip arthroplasty in the united states," *J. Bone Joint Surg. Am.*, vol. 91, p. 128–133, 2009.
- [9] W. H. Harris, "Wear and periprosthetic osteolysis: the problem," *Clin. Orthop. Relat. Res.*, no. 393, pp. 66-70, 2001.
- [10] A. Marshall, M. D. Ries and W. Paprosky, "How prevalent are implant wear and osteolysis, and how has the scope of osteolysis changed since 2000?," *J. Am. Acad. Orthop. Surg.*, vol. 16, no. suppl 1, pp. S1-6, 2008.

- [11] E. Garcia-Rey, E. García-Cimbrelo, A. Cruz and J. Ortega-Chamarro, "New types of polyethylene in total hip replacement: prospective and comparative clinical study on wear," *J. Bone Joint Surg. Br.*, vol. 91-B, no. SUPP II, p. 318, 2009.
- [12] J. Jacobs, N. Hallab, R. Urban and M. Wimmer, "Wear particles," *J. Bone Joint Surg. Am.*, vol. 88, no. suppl 2, p. 99, 2006.
- [13] A. Wang, A. Essner, V. K. Polineni, C. Stark and J. H. Dumbleton, "Lubrication and wear of ultra-high molecular weight polyethylene in total joint replacements," *Tribol. Int.*, vol. 31, no. 1-3, pp. 17-33, 1998.
- [14] J. Fisher, "Wear of ultra-high molecular weight polyethylene in total artificial joints," *Curr. Orthop.*, vol. 8, no. 3, p. 164, 1994.
- [15] H. McKellop, F. W. Shen, B. Lu, P. Campbell and R. Salovey, "Development of an extremely wear-resistant ultra high molecular weight polyethylene for total hip replacements," *J. Orthop. Res.*, vol. 17, no. 2, pp. 157-167, 1999.
- [16] H. McKellop, F. W. Shen, B. Lu, P. Campbell and R. Salovey, "Effect of sterilization method and other modifications on the wear resistance of acetabular cups made of ultra-high molecular weight polyethylene. A hip-simulator study," *J. Bone Joint Surg. Am.*, vol. 81-A, no. 12, pp. 1708-1725, 2000.
- [17] O. K. Muratoglu, C. Bragdon, D. O. O'Connor, M. Jasty and W. H. Harris, "A novel method of cross-linking ultra-high-molecular-weight polyethylene to improve wear, reduce oxidation, and retain mechanical properties," *J. Arthroplasty*, vol. 16, no. 2, pp. 149-60, 2001.
- [18] C. Heisel, M. Silva, M. A. dela Rosa and T. Schmalzried, "Short-term in vivo wear of cross-linked polyethylene," *J. Bone Joint Surg. Am.*, vol. 86-A, no. 4, pp. 748-751, 2004.
- [19] L. Bradford, R. Kurland, M. Sankaran, H. Kim, L. A. Pruitt and M. D. Ries, "Early failure due to osteolysis associated with contemporary highly cross-linked ultra-high molecular weight polyethylene. A case report," *J. Bone Joint Surg. Am.*, vol. 86-A, no. 5, pp. 1051-1056, 2004.
- [20] K. T. Mai, C. A. Verioti, K. Casey, Y. Slesarenko, L. Romeo and C. W. Colwell, "Cementless femoral fixation in total hip arthroplasty," *Am. J. Orthop.*, vol. 39, no. 3, pp. 126-130, 2010.
- [21] E. Gómez-Barrena, F. Medel and J. A. Puértolas, "Polyethylene oxidation in total hip arthroplasty: evolution and new advances," *Open Orthop. J.*, no. 3, pp. 115-120, 2009.

- [22] J. S. Siopack and H. E. Jergesen, "Total hip arthroplasty," *West J. Med.*, vol. 162, no. 3, p. 243–249, 1995.
- [23] I. D. Learmonth, C. Young and C. Rorabeck, "The operation of the century: total hip replacement," *The Lancet*, vol. 370, no. 9597, pp. 1508-1519, 2007.
- [24] P. F. Gomez and J. A. Morcuende, "Early attempts at hip arthroplasty—1700s to 1950s," *Iowa Orthop J.*, vol. 25, pp. 25-29, 2005.
- [25] M. N. Smith-Petersen, "Evolution of mould arthroplasty of the hip joint," *J. Bone Joint Surg. Br.*, vol. 30, no. 1, pp. 59-75, 1948.
- [26] Y.-S. Park, Y.-W. Moon, S.-J. Lim, J.-M. Yang, G. Ahn and Y.-L. Choi, "Early osteolysis following second-generation metal-on-metal hip replacement," *J. Bone Joint Surg. Am.*, vol. 87, no. 7, pp. 1515-1521, 2005.
- [27] L. Lidgren, "Chronic inflammation, joint replacement and malignant lymphoma," *J. Bone Joint Surg. Br.*, vol. 90, no. 1, pp. 7-10, 2008.
- [28] D. Ladon, A. Doherty, R. Newson, J. Turner, M. Bhamra and C. P. Case, "Changes in metal levels and chromosome aberrations in the peripheral blood of patients after metal-on-metal hip arthroplasty," *J. Arthroplasty*, vol. 19, no. 8 Suppl 3, pp. 79-83, 2004.
- [29] United States Food and Drug Administration, "Concerns about Metal-on-Metal Hip Implants," United States Food and Drug Administration, Silver Spring, Maryland, 2013.
- [30] B. Meier, "Concerns over 'Metal on Metal' hip implants," *New York Times*, 3 March 2010.
- [31] B. Meier, "As use of metal-on-metal hip implants grows, studies raise," *New York Times*, 3 March 2010.
- [32] C. J. Sychterz, C. A. Engh Jr., A. M. Young, R. H. Hopper Jr. and C. A. Engh, "Comparison of in vivo wear between polyethylene liners articulating with ceramic and cobalt-chrome femoral heads," *J. Bone Joint Surg. B.*, vol. 82, no. 7, pp. 948-951, 2000.
- [33] G. H. Isaac, C. Brockett, A. Breckon, D. V. D. Jagt, S. Williams, C. Hardaker, J. Fisher and A. Schepers, "Ceramic-on-metal bearings in total hip replacement: whole blood metal ion levels and analysis of retrieved components," *J. Bone Joint Surg. Br.*, vol. 91, no. 9, pp. 1134-1141, 2009.

- [34] A. J. Deshmukh, P. A. Rathod, W. H. Rodgers and J. A. Rodriguez, "Early failure of a ceramic-on-metal total hip arthroplasty: a case report," *JBJS Case Connector*, vol. 2, no. 2, pp. 1-6, 2012.
- [35] D. Dowson and Z.-M. Jin, "Metal-on-metal hip joint tribology," *P. I. Mech. Eng. H*, vol. 220, no. 2, pp. 107-118, 2006.
- [36] M. N. Rahaman, A. Yao, B. S. Bal, J. P. Garino and M. D. Ries, "Ceramics for prosthetic hip and knee joint replacement," *J. Am. Ceram. Soc.*, vol. 90, no. 7, pp. 1965-1988, 2007.
- [37] Z. M. Jin, D. Dowson and J. Fisher, "Analysis of fluid film lubrication in artificial hip joint replacements with surfaces of high elastic modulus," *P. I. Mech. Eng. H*, vol. 211, no. 3, pp. 247-256, 1997.
- [38] Z. M. Jin, J. B. Medley and D. Dowson, "Fluid film lubrication in artificial hip joints," *Tribology S.*, vol. 41, pp. 237-256, 2003.
- [39] K. Mai, C. Verioti, K. A. Ezzet, S. N. Copp, R. H. Walker and C. W. Colwell, "Incidence of 'squeaking' after ceramic-on-ceramic total hip arthroplasty," *Clin. Orthop. Relat. Res.*, vol. 468, no. 2, pp. 413-417, 2010.
- [40] W. L. Walter, T. S. Waters, M. Gillies, S. Donohoo, S. M. Kurtz, A. S. Ranawat, W. J. Hozack and M. A. Tuke, "Squeaking hips," *J. Bone Joint Surg.*, vol. 90, no. Suppl. 4, pp. 102-111, 2008.
- [41] J. C. Keurentjes, R. M. Kuipers, D. J. Wever and B. W. Schreurs, "High incidence of squeaking in THAs with alumina ceramic-on-ceramic bearings," *Clin. Orthop. Relat. Res.*, vol. 466, no. 6, pp. 1438-1443, 2008.
- [42] A. P. Sanders and R. M. Brannon, "Assessment of the applicability of the Hertzian contact theory to edge-loaded prosthetic hip bearings," *J. Biomech.*, vol. 44, no. 16, pp. 2802-2808, 2011.
- [43] I. Etsion, "State-of-the-art in laser surface texturing," *J. Tribol. T. ASME*, vol. 127, no. 1, pp. 248-253, 2005.
- [44] B. Raeymaekers, I. Etsion and F. E. Talke, "Enhancing tribological performance of the magnetic tape/guide interface by laser surface texturing," *Tribol. Lett.*, vol. 27, no. 1, pp. 89-95, 2007.
- [45] B. Raeymaekers, I. Etsion and F. Talke, "A model for magnetic tape/guide friction reduction by laser surface texturing," *Tribol. Lett.*, vol. 28, no. 1, pp. 9-17, 2007.

- [46] G. Ryk, Y. Kligerman and I. Etsion, "Experimental investigation of laser surface texturing for reciprocating automotive components," *Tribol. Trans.*, vol. 45, no. 4, pp. 444-449, 2002.
- [47] V. Brizmer, Y. Kligerman and I. Etsion, "A laser surface textured parallel thrust bearing," *Tribol. Trans.*, vol. 46, no. 3, pp. 397-403, 2003.
- [48] A. Chyr, M. Qiu, J. Speltz, R. L. Jacobsen, A. P. Sanders and B. Raeymaekers, "Patterned microtexture to reduce friction and wear and increase longevity of total hip replacement bearings," *Wear*, vol. 315, pp. 51-57, 2014.
- [49] H. Ito, K. Kaneda, T. Yuhta, I. Nishimura, K. Yasuda and T. Matsuno, "Reduction of polyethylene wear by concave dimples on the frictional surface in artificial hip joints," *J. Arthroplasty*, vol. 15, no. 3, pp. 332-338, 2000.
- [50] H. Sawano, S. I. Warisawa and S. Ishihara, "Study on long life of artificial joints by investigating optimal sliding surface geometry for improvement in wear resistance," *Prec. Eng.*, vol. 33, no. 4, p. 492-498, 2009.
- [51] X. Zhou, A. L. Galvin, Z. Jin, X. Yan and J. Fisher, "The influence of concave dimples on the metallic counterface on the wear of ultra-high molecular weight polyethylene," *P. I. Mech. Eng. J*, vol. 226, no. 6, pp. 455-462, 2011.
- [52] P. Bullough and J. Goodfellow, "The significance of the fine structure of articular cartilage," *J. Bone Joint Surg. B.*, vol. 50, no. 4, pp. 852-857, 1968.
- [53] G. Meachim and S. Roy, "Surface ultrastructure of mature adult human articular cartilage," *J. Bone Joint Surg. B.*, vol. 51, no. 3, pp. 529-539, 1971.
- [54] I. C. Clarke, "Articular cartilage: a review and scanning electron microscope study," *J. Bone Joint Surg. B.*, vol. 53, no. 4, pp. 732-750, 1971.
- [55] I. C. Clarke, D. J. Schurman and H. C. Amstutz, "In vivo and in vitro comparative studies of animal articular surfaces," *Ann. Biomed. Eng.*, vol. 3, pp. 100-110, 1975.
- [56] R. B. Longmore and D. L. Gardner, "The surface structure of ageing human articular cartilage: a study by reflected light interference microscopy (RLIM)," *J. Anat.*, vol. 126, no. 2, pp. 353-365, 1978.
- [57] E. D. Bonnevie, V. J. Baro, L. Wang and D. L. Burris, "Fluid load support during localized indentation of cartilage with a spherical probe," *J. Biomech.*, vol. 45, pp. 1036-1041, 2012.

- [58] R. B. Longmore and D. L. Gardner, "The surface structure of ageing human articular cartilage: a study by reflected light interference microscopy (RLIM)," *J. Anat.*, vol. 126, no. 2, pp. 353-365, 1978.
- [59] M. Qiu, A. Chyr, A. P. Sanders and B. Raeymaekers, "Prosthetic knee joints with bio-inspired bearing surfaces," *Tribol. Int.*, vol. 77, pp. 106-110, 2014.
- [60] D. Mazzucco, G. McKinley, R. Scott and M. Spector, "Rheology of joint fluid in total knee arthroplasty patient," *J. Orthop. Res.*, vol. 20, pp. 1157-1163, 2002.
- [61] A. Cooke, D. Dowson and V. Wright, "The rheology of synovial fluid and some potential synthetic lubricants for degenerate synovial fluid," *Eng. Med.*, vol. 7, no. 2, pp. 66-72, 1978.
- [62] Z. Jin, D. Dowson and J. Fisher, "Analysis of fluid film lubrication in artificial hip joint replacements with surfaces of high elastic modulus," *Proc. Inst. Mech. Eng. H.*, vol. 211, no. 3, pp. 247-256, 1997.
- [63] O. Pinkus and B. Sternlicht, *Theory of Hydrodynamic Lubrication*, New York: McGraw-Hill, 1961.
- [64] M. Qiu, B. R. Minson and B. Raeymaekers, "The effect of texture shape on the load-carrying capacity of gas-lubricated parallel slider bearings," *Tribol. Lett.*, vol. 48, no. 3, pp. 315-327, 2012.
- [65] M. Qiu, A. Delic and B. Raeymaekers, "The effect of texture shape on the load carrying capacity of gas lubricated parallel slider bearings," *Tribol. Lett.*, vol. 48, no. 3, pp. 315-328, 2012.
- [66] A. Shinkarenko, Y. Kligerman and I. Etsion, "The effect of surface texturing in soft elasto-hydrodynamic lubrication," *Tribol. Int.*, vol. 42, no. 2, pp. 284-292, 2009.
- [67] M. R. Gevaert, M. LaBerge, J. M. Gordon and J. D. DesJardins, "The quantification of physiologically relevant cross-shear wear phenomena on orthopaedic bearing materials using the MAX-shear wear testing system," *J. Tribol. - T. ASME*, vol. 127, no. 4, pp. 740-749, 2005.
- [68] G. W. Blunn, P. S. Walker, A. Joshi and K. Hardinge, "The dominance of cyclic sliding in producing wear in total knee replacements," *Clin. Orthop. Relat. Res.*, vol. 273, p. 253-260, 1991.
- [69] C. R. Bragdon, D. O. O'Connor, J. D. Lowenstein, M. Jasty and W. D. Syniuta, "The importance of multidirectional motion on the wear of polyethylene," *Proc. Inst. Mech. Eng., Part H: J. Eng. Med.*, vol. 210, no. H3, p. 157-165, 1996.

- [70] A. Wang, C. Stark and J. H. Dumbleton, "Mechanistic and morphological origins of ultra-high molecular weight polyethylene wear debris in total joint replacement prostheses," *P. I. Mech. Eng. H.*, vol. 210, no. H3, p. 141–155, 1996.
- [71] V. Saikko, "A multidirectional motion pin-on-disk wear test method for prosthetic joint materials," *J. Biomed. Mater. Res.*, vol. 41, no. 1, p. 58–64, 1998.
- [72] S. A. Atwood, D. W. Van Citters, E. W. Patten, J. Furmanski, R. M. D. and P. L. A., "Tradeoffs amongst fatigue, wear, and oxidation resistance of cross-linked ultra-high molecular weight polyethylene," *J. Mech. Behav. Biomed.*, vol. 4, no. 7, pp. 1033-1045, 2011.
- [73] C. R. Bragdon, D. O. O'Connor, J. D. Lowenstein, M. Jasty, S. A. Biggs and W. H. Harris, "A new pin-on-disk wear testing method for simulating wear of polyethylene on cobalt-chrome alloy in total hip arthroplasty," *J. Arthroplasty*, vol. 16, no. 5, p. 658–665, 2001.
- [74] T. J. Joyce, C. Vandelli, T. Cartwright and A. Unsworth, "A comparison of the wear of cross-linked polyethylene against itself under reciprocating and multi-directional motion with different lubricants," *Wear*, vol. 250, no. 1-12, pp. 206-211, 2001.
- [75] A. Wang, "A unified theory of wear for ultra-high molecular weight polyethylene in multi-directional sliding," *Wear*, vol. 248, no. 1-2, pp. 38-47, 2000.
- [76] T. M. McGloughlin and A. G. Kavanagh, "Wear of ultra-high molecular weight polyethylene (UHMWPE) in total knee prostheses: a review of key influences," *P. I. Mech. Eng. H.*, vol. 214, no. H4, p. 349–359, 2000.
- [77] D. Zhao, H. Sakoda, G. W. Sawyer, S. A. Banks and B. J. Fregly, "Predicting knee replacement damage in a simulator machine using a computational model with a consistent wear factor," *J. Biomech. Eng. - T. ASME*, vol. 130, no. 1, p. 011004, 2008.
- [78] E. S. Grood and W. J. Suntay, "A joint coordinate system for the clinical description of three-dimensional motions: application to the knee," *J. Biomech. Eng.*, vol. 105, no. 2, pp. 136-144, 1983.
- [79] P. Komdeur, F. E. Pollo and R. W. Jackson, "Dynamic knee motion in anterior cruciate impairment: a report and case study," *Proc. (Bay. Univ. Med. Cent.)*, vol. 15, no. 3, pp. 257-259, 2002.
- [80] *Implants for surgery—wear of hip joint prostheses—Part 1: Loading and displacement parameters for wear testing machines and corresponding environmental conditions for test*, ISO Standard 14242-1:2012.

- [81] M. Nordin and V. H. Frankel, "Biomechanics of the knee, Chapter 7," in *Basic Biomechanics of the Musculoskeletal System*, 3rd ed., M. Nordin and V. H. Frankel, Eds., Baltimore, MA, Lippincott, Williams and Wilkins, 2001.
- [82] P. S. Walker, "Biomechanics of total knee replacement designs, Chapter 15," in *Basic Orthopaedic Biomechanics & Mechano-biology*, 3rd ed., V. Mow and R. Huiskes, Eds., Philadelphia, PA, Lippincott, Williams and Wilkins, 2004, pp. 657-702.
- [83] K. L. Johnson, *Contact mechanics*, Cambridge: Cambridge University Press, 1987.
- [84] D. L. Bartel, V. L. Bicknell and T. M. Wright, "The effect of conformity, thickness, and material on stresses in ultra-high molecular weight components for total joint replacement," *J. Bone Joint Surg. Am.*, vol. 66, no. 7, pp. 1041-1051, 1986.
- [85] H. Haider, "Tribological assessment of UHMWPE in the knee, Chapter 26," in *UHMWPE Biomaterials Handbook*, 2nd ed., S. M. Kurtz, Ed., San Diego, CA, Academic Press, 2009, pp. 381-408.
- [86] S. A. V. Swanson, M. A. R. Freeman and J. C. Heath, "Laboratory tests on total joint replacement prosthesis," *J. Bone Joint Surg. Br.*, vol. 55, no. 4, pp. 759-773, 1973.
- [87] D. Dowson, B. Jobbins, J. O'Kelly and V. Wright, "A knee joint simulator, Chapter 7," in *Evaluation of Artificial Hip Joints*, UK Biological Engineering Society, 1977, pp. 79-90.
- [88] M. J. Pappas and F. F. Buechel, "New Jersey knee simulator," in *Trans. of the 11th Annu. Int. Biomater. Symp.*, 1979.
- [89] M. J. Pappas and F. F. Buechel, "On the use of constraint radius femoral component in meniscal bearing knee replacement.," *J. Orthop. Rheumatol.*, vol. 7, pp. 27-29, 1994.
- [90] I. C. Burgess, M. Kolar, J. L. Cunningham and A. Unsworth, "Development of a six station knee wear simulator and preliminary wear results," *P. I. Mech. Eng. H.*, vol. 211, no. 1, pp. 37-47, 1997.
- [91] P. S. Walker, G. W. Blunn, D. R. Broome, J. Perry, A. Watkins, S. Sathasivam, M. E. Dewar and J. P. Paul, "A knee simulating machine for performance evaluation of total knee replacements," *J. Biomech.*, vol. 30, no. 1, pp. 83-89, 1997.

- [92] *Implants for surgery—wear of total knee joint prostheses—Part 1: loading and displacement parameters for wear testing machines with load control and corresponding environmental conditions for test*, ISO Standard 14243-1:2009.
- [93] K. Kawanabe, I. C. Clarke, J. Tamura, M. Akagi, V. D. Good, P. A. Williams and K. Yamamoto, "Effects of A–P translation and rotation on the wear of UHMWPE in a total knee joint simulator," *J. Biomed. Mater. Res.*, vol. 54, no. 3, pp. 400-406, 2000.
- [94] P. I. Barnett, H. M. McEwen, D. D. Auger, M. H. Stone, E. Ingham and J. Fisher, "Investigation of wear of knee prostheses in a new displacement/force-controlled simulator," *P. I. Mech. Eng. H.*, vol. 216, no. 1, pp. 51-61, 2002.
- [95] *Implants for surgery—wear of knee joint prostheses—Part 3: Loading and displacement parameters for wear-testing machines with displacement control and corresponding environmental conditions for test*, ISO Standard 14243-3:2009.
- [96] Y. S. Liao, P. D. Benya and H. A. McKellop, "Effect of protein lubrication on the wear properties of materials for prosthetic joints," *J. Biomed. Mater. Res.*, vol. 48, no. 4, pp. 465-473, 1999.
- [97] *Implants for surgery—wear of total hip joint prostheses—Part 2: methods of measurement*, ISO Standard 14242-2:2012.
- [98] A. Chyr, A. Sanders and B. Raeymaekers, "A hybrid apparatus for friction and accelerated wear testing of total knee replacement bearing materials," *Wear*, vol. 308, pp. 54-60, 2013.
- [99] A. P. Sanders and R. M. Brannon, "Determining a surrogate contact pair in a Hertzian contact problem," *J. Trib. T. - ASME*, vol. 133, no. 2, p. 024502, 2011.
- [100] B. J. Hamrock, S. R. Schmid and B. O. Jacobson, *Fundamentals of Fluid Film Lubrication*, New York: CRC Press, 2004.
- [101] R. Tsukamoto, S. Chen, T. Asano, M. Ogino, H. Shoji, T. Nakamura and I. C. Clarke, "Improved wear performance with crosslinked UHMWPE and zirconia implants in knee simulation," *Acta Orthop.*, vol. 77, no. 3, p. 505–511, 2006.
- [102] Y. P. Shkolnikov, A. Bowden, D. MacDonald and S. Kurtz, "Wear pattern observations from TDR retrievals using autoregistration of voxel data," *J. Biomed. Mater. Res. B Appl. Biomater.*, vol. 94, no. 2, pp. 312-317, 2010.

- [103] J. Q. Yao, M. P. Laurent, T. S. Johnson, C. R. Blanchard and R. D. Crowninshield, "The influences of lubricant and material on polymer/CoCr sliding friction," *Wear*, vol. 255, no. 1-6, pp. 780-784, 2003.
- [104] J. D. DesJardins, A. Aurora, S. L. Tanner, T. B. Pace and D. M. Laberge, "Increased total knee arthroplasty ultra-high molecular weight polyethylene wear using a clinically relevant hyaluronic acid simulator lubricant," *P. I. Mech. Eng. H.*, vol. 220, no. 5, pp. 609-623, 2006.
- [105] *Standard test method for wear testing of polymeric materials used in total joint prostheses*, ASTM Standard F732-00:2011.
- [106] Y. Schneider, "Formation of surfaces with uniform micropatterns on precision machine and instruments parts," *Precis. Eng.*, vol. 6, no. 4, pp. 219-225, 1984.
- [107] X. Wang and K. Kato, "Improving the anti-seizure ability of SiC seal in water with RIE texturing," *Tribol. Lett.*, vol. 14, no. 4, pp. 275-280, 2003.
- [108] M. Wakuda, Y. Yamauchi, S. Kanzaki and Y. Yasuda, "Effect of surface texturing on friction reduction between ceramic and steel materials under lubricated sliding contact," *Wear*, vol. 254, no. 3-4, pp. 356-363, 2003.
- [109] U. Pettersson and S. Jacobson, "Influence of surface texture on boundary lubricated sliding contacts," *Tribol. Int.*, vol. 36, no. 11, pp. 857-864, 2002.
- [110] L. S. Stephens, R. Siripuram, M. Hayden and B. McCartt, "Deterministic micro asperities on bearings and seals using a modified LIGA process," *J. Eng. Gas Turb. Power*, vol. 126, no. 1, pp. 147-154, 2004.
- [111] A. Greco, C. Lin, S. Raphaelson, K. Ehmann and Q. J. Wang, "Surface texturing of tribological interfaces using the vibromechanical texturing method," *J. Manf. Sci. Eng.*, vol. 131, no. 6, pp. 1-8, 2009.
- [112] D. Scott, M. Brandt and B. Dorien-Brown, "Laser modification of metal surfaces," *Opt. Laser Eng.*, vol. 18, no. 1, pp. 1-13, 1993.
- [113] G. Dumitru, V. Romano, H. Weber, H. Haefke, Y. Gerbig and E. Pflüger, "Laser microstructuring of steel surfaces for tribological applications," *Appl. Phys A-Mater.*, vol. 70, no. 4, pp. 485-487, 2000.
- [114] G. Duffeta, P. Sallamanda and A. Vannes, "Improvement in friction by cw Nd:YAG laser surface treatment on cast iron cylinder bore," *Appl. Surf. Sci.*, vol. 205, no. 1-4, pp. 289-296, 2003.

- [115] A. Erdemir, "Review of engineered tribological interfaces for improved boundary lubrication," *Tribol. Int.*, vol. 38, no. 3, pp. 249-256, 2005.
- [116] L. Vilhena, M. Sedlaček, B. Podgornik, J. Vižintin, A. Babnik and J. Možina, "Surface texturing by pulsed Nd:YAG laser," *Tribol. Int.*, vol. 42, no. 10, pp. 1496-1504, 2009.
- [117] S. Woods, "Understanding scanning white light interferometry," *MICROmanufacturing*, vol. 2, no. 4, December 2009.
- [118] M. Johnson, "'White light' interferometry," *Proc. SPIE*, vol. 1314, pp. 307-314, 1990.
- [119] J. S. Lim, *Two-Dimensional Signal and Image Processing*, Englewood Cliffs, NJ: Prentice Hall, 1990.
- [120] W. A. Hodge, R. S. Fijan, K. L. Carlson, R. G. Burgess, W. H. Harris and R. W. Mann, "Contact pressures in the human hip joint measured in vivo," *P. Natl. Acad. Sci. USA*, vol. 83, no. 9, pp. 2879-2883, 1986.
- [121] D. E. Krebs, L. Elbaum, P. O. Riley, W. A. Hodge and R. W. Mann, "Exercise and gait effects on in vivo hip contact pressures," *Phys. Ther.*, vol. 71, no. 4, pp. 301-309, 1991.
- [122] M. P. Murray, A. B. Drought and R. C. Kory, "Walking patterns of normal men," *J. Bone Joint Surg.*, vol. 46, no. 2, pp. 335-360, 1964.
- [123] F. Gustafsson, "Determining the initial states in forward-backward filtering," *Signal Processing, IEEE Transactions*, vol. 44, no. 4, pp. 998-992, 1996.